GEOCHEMISTRY

Onset of slab mantle melting in Earth's lower mantle: Evidence from ferropericlase in superdeep diamonds

Peng Ni[1,2]*, Steven B. Shirey[2], Michael J. Walter[2], Janina Czas[2], Davide Novella[3], Fabrizio Nestola[3], Nico Kueter[2,4], Evan M. Smith[5], Thomas Stachel[6], D. Graham Pearson[6], Andrew Steele[2], Laura L. Gardner[7], Steven D. Jacobsen[7], Ben Harte[8], Jeffrey W. Harris[9], Anat Shahar[2]

Ferropericlase ([Mg_x,Fe_{1-x}]O), the most common inclusion in sublithospheric diamonds, has a poorly understood crystallization history and depth of origin. Nineteen microscopic ferropericlase grains with different Mg#s were released from Juína and Kankan diamonds with mantle-like carbon, for Mg and Fe isotopic analysis. Two groups of ferropericlase inclusions can be distinguished with respect to diamond growth: high-Mg# inclusions with mantle-like Mg and Fe ($\delta^{26}Mg = -0.23 \pm 0.22‰$; $\delta^{56}Fe = 0.00 \pm 0.14‰$) inferred to be preexisting and lower Mg# inclusions with non–mantle-like heavy Fe ($\delta^{56}Fe$ up to +0.3‰) and light Mg ($\delta^{26}Mg$ down to −1.4‰) inferred to be coeval. We propose that coeval ferropericlase inclusions formed by melting of hydrated and carbonated peridotitic slab components subducted to lower mantle depths. Continuous reaction of these melts with surrounding reduced, dry slab harzburgite can produce the large range in Mg# and Ni contents of our ferropericlase suite—a heretofore unexplained feature of global ferropericlase data.

INTRODUCTION

Plate tectonics can change the composition, mineralogy, and physical properties of the deep Earth by volatile element (H, C, O, and S) and halogen (Cl, F) transport into the mantle during slab subduction. Oceanic island arcs provide ample evidence of fluid release at sub-arc depths: seismic activity derived by dehydration embrittlement (*1*), fluid escape along the subduction channel (*2*), lowering of the mantle solidus and thus enhanced melting in the mantle wedge (*3*), and eruption of some of Earth's most water-rich magmas (*4*). These observations provide direct evidence that subducting plates carry volatile elements and halogens derived from hydrothermal interaction with seawater to at least 250-km depths in the mantle (*5*). Subduction recycling of surface volatiles is also evidenced by studies focusing on ocean island basalts (OIBs) [e.g., (*6*, *7*)].

Until recently, it was thought that beyond ~250 km, subducting plates would be stripped of their volatiles (*8*, *9*). However, studies in mantle tomography (*10*), seismology (*11*), diamond petrology (*12*, *13*), and thermal modeling/geodynamics (*14*) demonstrate that older and hence colder oceanic plates can carry volatiles to uppermost lower mantle depths (700 to 800 km)—a region where released fluids can cause sublithospheric diamonds to form (*14*).

Sublithospheric diamonds and their mineral cargo provide an unparalleled opportunity to examine volatile transport and their deep release. Diamonds grow at depth from the reduction of C-bearing fluids and melts (hereafter "fluids") by the mantle (*15*). They are Earth's deepest-formed mantle samples and have been transported back to the surface by mantle convection and rapidly erupting kimberlitic magmas. During growth, diamond may encapsulate preexisting minerals either from the mantle host or coeval minerals growing from the fluid. However, once formed, diamond is stable throughout the entire mantle below ~150-km depth (*16*), preserving the trapped inclusions. The exceptionally low elemental diffusivities in diamond make it unreactive with the solid mantle host and able to shield included minerals from chemical reequilibration during mantle convection and kimberlite eruption.

This study reports Fe and Mg isotopic composition of a main mineralogical constituent of Earth's lower mantle, ferropericlase. Ferropericlase, which occurs with bridgmanite and Ca silicate perovskite in lower mantle peridotite, is also the most abundant inclusion in many sublithospheric diamond suites. In addition to establishing the Fe and Mg isotopic composition of ferropericlase inclusions to explore their petrogenesis, the purpose of this paper is to better constrain the sources of the deep fluids/melts responsible for forming the sublithospheric diamonds in the uppermost lower mantle, to show how the fluids could be released, and to explore their role in modifying the deep mantle. Answers to these questions are important for understanding the phase changes and deformation occurring in deeply subducted plates, the onset of melting in the slab mantle, the nature of Earth's deep mantle volatile cycle, the generation of deep-focus earthquakes, and the creation of heterogeneity at mid-mantle levels.

Sublithospheric diamonds for this study come from two well-studied alluvial localities, Juína, Brazil, and Kankan, Guinea. Both localities have figured prominently in our understanding of sublithospheric diamonds and their mineral inclusions [see historical summary in (*15*)]. At the Juína locality, numerous studies have demonstrated the existence of mantle transition zone and lower mantle assemblages and how they formed (*13*, *17*–*29*). For the Kankan locality, Stachel *et al.* (*30*–*32*) specifically traced mantle mineralogy from the lithosphere to the lower mantle.

Alluvial sublithospheric diamonds from the Juína area are thought to have been supplied by the weathering of the Juína 5 and Collier 4 kimberlite pipes and many other unexposed kimberlites of similar

[1]Department of Earth, Planetary, and Space Sciences, University of California, Los Angeles, Los Angeles, CA 90095, USA. [2]Earth and Planets Laboratory, Carnegie Science, Washington, DC 20015, USA. [3]Department of Geosciences, University of Padua, Via G. Gradenigo 6, 35131 Padua, Italy. [4]Geological Institute, ETH Zürich, Sonneggstrasse 5, Zurich, Switzerland. [5]Gemological Institute of America, New York, NY 10036, USA. [6]Department of Earth and Atmospheric Sciences, University of Alberta, Edmonton, Alberta T6G 2E3, Canada. [7]Department of Earth and Planetary Sciences, Northwestern University, 2145 Sheridan Rd., Evanston, IL 60208, USA. [8]Department of Geology and Geophysics, University of Edinburgh, Edinburgh EH93JW, UK. [9]School of Geographical and Earth Sciences, University of Glasgow, G12 8QQ Glasgow, UK.
*Corresponding author. Email: pengni@epss.ucla.edu

Cretaceous age in the region. These kimberlites erupted through a Proterozoic mobile belt at the southwestern margin of the Archean Amazonian composite craton—a similar mobile belt geologic setting to the Ellendale and Argyle localities in northwestern Australia. Such mobile belts are now considered to be deformed, younger, marginal parts of composite cratons that have become "cratonized" to make supercratons (*33*) by the addition of thickened lithospheric mantle. What sets Juína apart as a locality is the very large percentage of sublithospheric versus lithospheric diamonds as evidenced by an overwhelming number of low-N, type II diamonds. Ferropericlase inclusions for this study come from type II diamonds purchased on collecting trips to the town of Juína in 2014 and 2019, as well as samples previously reported on by Harte and coworkers (*18*, *34*).

Alluvial diamonds mined in Guinea [see summaries in (*32*–*34*)] are thought to come from known early Cretaceous kimberlite clusters at Banankoro in the Mandala Basin (*35*) and other unexposed, similar-aged kimberlites. Kimberlites in this region erupted through the Meso- to Neoarchean Man cratonic nucleus, now part of the West Africa composite craton (*33*). Xenoliths from the subcontinental lithospheric mantle of the Man craton carry the characteristic signatures of melt depletion generally seen in Archean nuclei (*36*). Ferropericlase inclusions for this study come from the diamond suites studied by Stachel (*30*–*32*) that were purchased in the provincial capital of Kankan (*30*). They were obtained as released, isolated grains from previously studied diamonds.

For Juína, it has been proposed that the diamonds were erupted to the surface by kimberlites in the Cretaceous, perhaps related to the 109-million-year-old Trindade plume (*21*, *23*), whereas for Kankan no link between kimberlites and a mantle plume has been suggested. However, Aulbach *et al.* (*37*) recently proposed a plume source for the Koidu, Liberia kimberlites, and Gernon *et al.* (*38*) suggested that kimberlites were generated from the subcontinental lithospheric mantle at rift edges (e.g., Brazil and Guinea) as a natural, postrift consequence of the type of rifting that created the Atlantic Ocean.

The Juína and Kankan diamonds crystallized in the Cambrian as shown by the recent Rb-Sr, Sm-Nd, U-Pb, and Re-Os geochronological studies of breyite and larnite (retrogressed Ca-silicate perovskite) and pyrrhotite by Timmerman and coworkers (*39*). The most likely setting for sublithospheric diamond formation in the Cambrian appears to be a subduction zone around the northwestern margin of the Gondwana supercontinent (*39*). This system is thought to have carried volatiles to the deep upper mantle and transition zone where diamond-forming fluids were released and reduced, crystallizing diamonds. Buoyancy of the thermally equilibrated metaperidotitic diamond substrates enabled the transportation of diamonds upward to the base of the supercontinent keel where they were stored in the lithospheric root, moving with the supercontinent until its initial break-up in the Jurassic (*39*, *40*). This common history of the Juína and Kankan localities allows us to investigate them together for a more thorough look at the evolution of slab-derived fluid during diamond growth.

RESULTS

Ferropericlase composition

Ferropericlase inclusions analyzed in this study have Mg#s [Mg/(Mg + Fe_t) in atomic ratio] of 0.58 to 0.81 for those from Juína, Brazil ($n = 14$), and 0.85 to 0.88 for those from Kankan, Guinea ($n = 5$). Images of one of the ferropericlase inclusions from Juína are shown in Fig. 1 as an example. Four additional ferropericlase inclusions from Juína with Mg# of 0.61, 0.64, 0.78, and 0.85 were exposed but no Fe or Mg isotope data were obtained. The five ferropericlase inclusions from Kankan have similar chemical composition (in wt %), with 1.28 to 1.46 NiO, 0.34 to 0.57 Cr_2O_3, 0.16 to 0.22 MnO, and <0.34 Na_2O. The ferropericlase inclusions from Juína show a broader range of minor element composition, with 0.32 to 1.39 NiO, 0.20 to 0.87 Cr_2O_3, 0.14 to 0.69 MnO, and 0.01 to 0.99 Na_2O (table S1).

The major element composition of ferropericlase inclusions selected for this study is generally consistent with ferropericlase from other studies (*41*). A positive correlation between NiO and Mg# and negative correlation between MnO and Mg# are observed, whereas Cr_2O_3 and Na_2O do not appear to show correlations with Mg# (fig. S1). Essentially all ferropericlase that we analyzed with Mg# lower than 0.80 originated from the Amazonian craton (*42*).

Carbon isotope composition

Twelve diamonds containing ferropericlase (Mg# > 0.50) or magnesiowütite (Mg# < 0.50) inclusions from Juína, Brazil were analyzed for their bulk carbon isotopic composition. Duplicate analyses of two chips from the same diamond (6b05) yielded results within analytical error from each other (table S2). The $\delta^{13}C$ composition

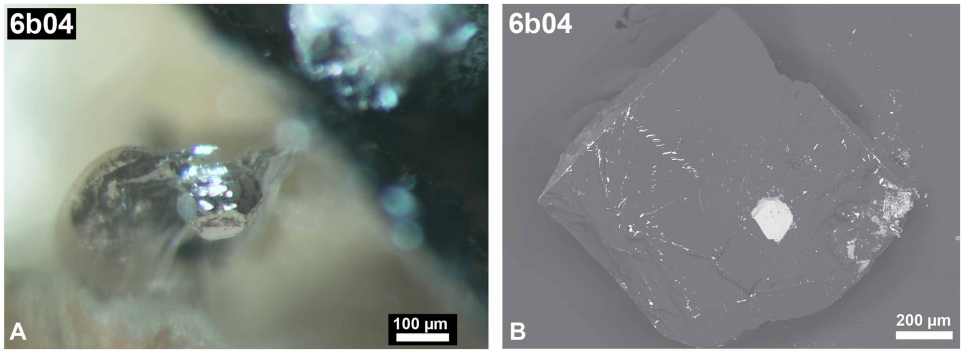

Fig. 1. Images of a ferropericlase inclusion in diamond. (**A**) Microscopic image of the inclusion before exposure. The inclusion is surrounded by a disc-shaped fracture partially filled with graphite. (**B**) Backscattered electron image of the inclusion in the host diamond after exposure. The surface morphology of the inclusion was partially preserved. The diamond surface was cleaned before dissolution of the inclusion.

(defined as the per mil difference in $^{13}C/^{12}C$ ratio relative to the Vienna-Pee Dee Belemnite) of the diamonds form a narrow range of −5.70 ± 0.09‰ (2 SD) to −4.39 ± 0.09‰, with an average $\delta^{13}C$ of −4.92 ± 0.68‰ (2 SD) that is indistinguishable from the mantle value of −5‰ (*43*).

Iron isotope composition

Seventeen ferropericlase inclusions from Kankan and Juína were analyzed for their iron isotopic composition (table S3). Extraction/dissolution of the inclusions typically yielded 0.3 to 3 μg of Fe each, except for the one in diamond AZ1_2 from Juína with 10.6 μg of Fe. Iron isotopic compositions of the ferropericlase are reported as both $\delta^{56}Fe$ and $\delta^{57}Fe$ ($^{56}Fe/^{54}Fe$ or $^{57}Fe/^{54}Fe$ ratio relative to IRMM-014 in per mil unit). Later discussions, however, will focus on $\delta^{56}Fe$ since ^{56}Fe is more abundant and hence easier to measure precisely for small samples. Repeat analyses of a ferropericlase inclusion in diamond N5a from Juína, on the same aliquot of purified Fe and duplicated column purifications yielded $\delta^{56}Fe$ values of −0.013 ± 0.042‰ (2 SE), −0.004 ± 0.044‰, and −0.043 ± 0.024‰, which are within analytical error from each other. Similarly, duplicate column purification for inclusions in diamonds JH17A1 and JH12A1 also yielded $\delta^{56}Fe$ values within analytical error from each other (table S3).

The four ferropericlase inclusions from Kankan show a narrow range of $\delta^{56}Fe$ compositions between −0.039 ± 0.052‰ and 0.076 ± 0.038‰ (2 SE), which is within analytical error of the mantle iron isotopic composition estimated on the basis of mantle peridotite data [$\delta^{56}Fe$ = 0.03‰; (*3*, *4*)]. Conversely, ferropericlase inclusions from Juína exhibit a much wider range of Fe isotopic compositions with $\delta^{56}Fe$ varying from −0.255 ± 0.036‰ to 0.242 ± 0.022‰ (2 SE). The isotopic variation is comparable to the whole range of $\delta^{56}Fe$ values reported for mantle peridotites, mid-ocean ridge basalts (MORBs), OIBs, and island-arc basalts (Fig. 2). Such light and heavy iron isotope compositions measured for ferropericlase inclusions in Juína diamonds are distinct from those from Kankan.

Magnesium isotope composition

The ferropericlase inclusions each contain 0.5 to 3 μg pf Mg. Isotopic analyses yielded compositions of −0.105 ± 0.032‰ (2 SE) to −1.440 ± 0.038‰ in $\delta^{26}Mg$. The two ferropericlase from Kankan have $\delta^{26}Mg$ values of −0.105 ± 0.032‰ and −0.178 ± 0.056‰, slightly heavier than the well-constrained mantle composition of −0.25 ± 0.07‰ (2 SD) (*44*). In contrast, magnesium in Juína ferropericlase inclusions appears to be isotopically lighter than the mantle value, with most of the inclusions being −0.3 to −0.4‰ in $\delta^{26}Mg$ (Fig. 3). In particular, two of the ferropericlases (JH17A1 and BZ70) have $\delta^{26}Mg$ compositions of −0.545 ± 0.040‰ and −1.440 ± 0.038‰, substantially lower than the mantle value. The large range of magnesium isotope compositions measured for the ferropericlase inclusions in sublithospheric diamonds is in strong contrast with primitive peridotite xenoliths and oceanic basalts. Mantle peridotites, MORBs, and OIBs were reported to have highly similar magnesium isotope compositions, with similar mean values of −0.24 ± 0.04‰ (2 SD), −0.25 ± 0.06‰, and −0.26 ± 0.08‰, respectively (Fig. 3) (*44*).

DISCUSSION

Experimental petrologic and seismologic studies indicate that the phase change from ringwoodite to bridgmanite + ferropericlase

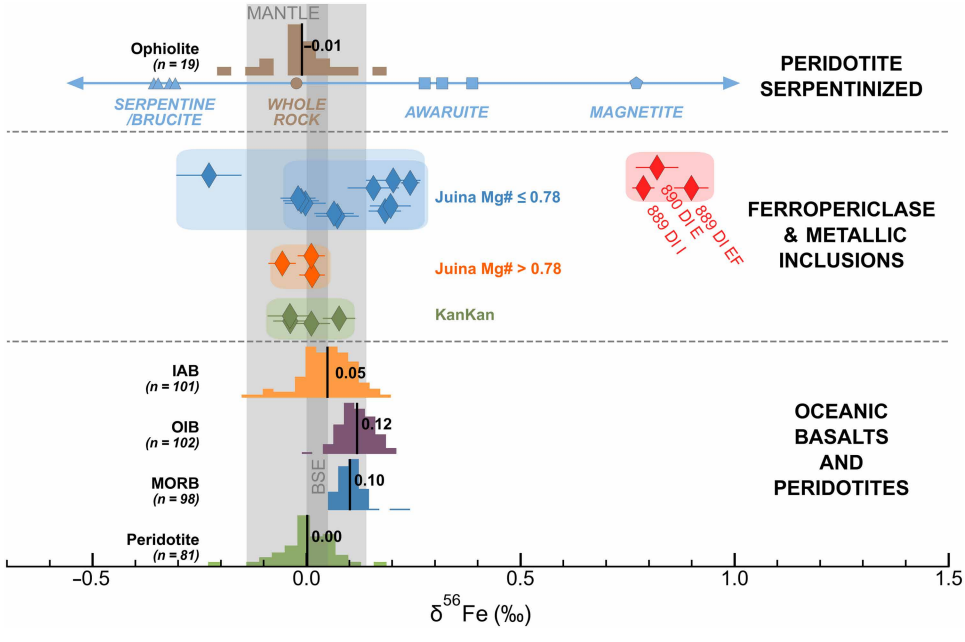

Fig. 2. Iron isotope results. High-Mg ferropericlase inclusions from Kankan and Juína show a narrow range of iron isotopic composition, near the bulk silicate Earth value of 0.03‰, whereas low-Mg ferropericlase from Juína show a larger range, extending mostly toward the heavy side. Iron isotope data for metallic inclusions in CLIPPIR diamonds from (*53*) are shown in red diamonds. Error bars represent 2 SEM. Iron isotope data for peridotites, MORB, OIBs, and island arc basalts (IAB) are from (*59*, *103*–*114*). The dark gray region represents the estimated composition for the bulk silicate Earth (*59*, *60*). The light gray region depicts the iron isotope compositional range of peridotites (0.00 ± 0.14‰, 2 SD), whose data span is largely due to serpentinization. Data for ophiolites and mineral separates in serpentinized peridotite are from (*88*, *115*). Figure modified from (*53*), licensed under CC BY 4.0 (http://creativecommons.org/licenses/by/4.0/). Changes include data addition and minor restyling.

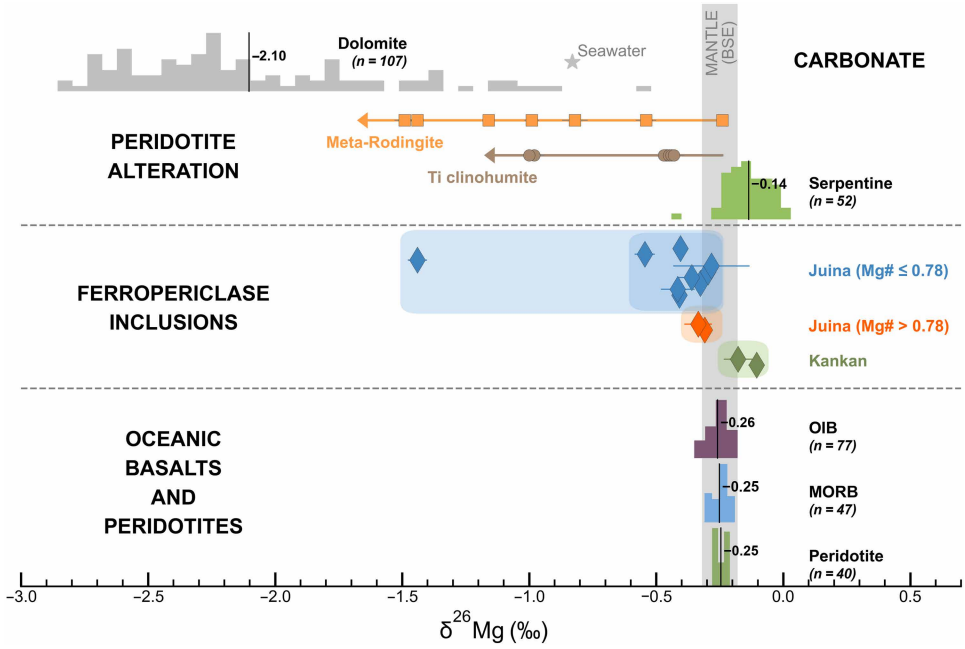

Fig. 3. Magnesium isotope results. The two ferropericlase inclusions from Kankan are slightly heavy in Mg isotopic composition. The two high-Mg# ferropericlase inclusions from Juína are mantle-like in δ^{26}Mg, whereas the low-Mg# ones demonstrate a clear tendency toward light Mg isotope composition. Error bars represent 2 SEM. Peridotites, MORBs, and OIBs have highly consistent Mg isotope compositions that define a Bulk Silicate Earth (BSE) δ^{26}Mg value of −0.25 ± 0.07‰ (2 SD) (*44*). Because of the limited variations in peridotite data, the mantle compositional range defined by the peridotite is identical to BSE. Magnesium isotope composition of the seawater is from (*116*). Magnesium isotope data for sedimentary dolomites from (*117*–*124*) are used to demonstrate the characteristic light Mg isotope composition of Mg-bearing carbonates, due to the lack of Mg isotope data for carbonates in serpentinized peridotites and basalts. Magnesium isotope data for peridotite metasomatism phases (meta-rodingites and Ti clinohumite) are from (*79*).

assemblages marks the mantle transition zone–lower mantle boundary (*45*–*47*). Geodynamic models of cold slab mantle subduction (*48*, *49*) provide the mineralogical mechanisms to transport volatiles that can promote sublithospheric diamond formation in the lower mantle, supporting the idea that ferropericlase inclusions in sublithospheric diamonds can be lower mantle phases. However, since ferropericlase is also known to be stable at shallower levels in the upper mantle, it is not clear that the ferropericlase is of lower mantle origin from the inclusion itself (*29*, *50*, *51*). Thus, we used an approach that combines the stable isotope systems of C, Fe, and Mg with previous observations on crystallographic relationships and inclusion coexistence to better understand the origin of ferropericlase inclusions.

Isotopes of carbon have been a powerful tool for tracing the origin of diamonds because in supercritical fluids at deep mantle temperatures and in open systems, C isotopic variation due to fractionation is much less than the range of C composition in various C sources (*43*). The well-known C isotope database for geological materials demonstrates a mantle with $\delta^{13}C \approx -5‰$, seawater-derived carbonates that are high in $^{13}C/^{12}C$ ratios ($\delta^{13}C \approx 0‰$) and reduced organic carbon as low as $<-25‰$ in $\delta^{13}C$. The well-established observation of ^{13}C-depletion signatures in eclogitic (E-type) lithospheric and majoritic garnet bearing transition zone diamonds can be attributed to the subduction of altered oceanic crust (*52*). Nitrogen isotope measurements, coupled with carbon isotopes, could be more diagnostic of the source for lithospheric diamonds (*43*), but sublithospheric diamonds are often too low in N (i.e., type II diamonds that contain low or undetectable nitrogen) for accurate isotopic analyses.

The iron and magnesium isotopic compositions of mantle-derived silicate rocks are relatively homogeneous, but a large magnitude of fractionation occurs in low-temperature environments. Extremely heavy iron isotopic compositions have been reported for metallic inclusions in a group of so-called CLIPPIR diamonds, which were attributed to Fe-rich phases produced during peridotite serpentinization on the ocean floor at relatively low temperatures (*53*). No Mg isotopic analysis has been previously reported for inclusions in sublithospheric diamonds. However, the characteristically light Mg isotope signature of carbonates, regardless of their origin, contrasts with the highly homogeneous Mg isotopic compositions found in seawater, MORBs, peridotite xenoliths, and OIBs, making the Mg isotope system a potential indicator for the involvement of carbonates during diamond formation (*54*). Therefore, Fe and Mg isotope compositions of ferropericlase inclusions can be combined with carbon isotopes to provide a previously unexplored perspective on the source of diamond-forming fluids and the mineralogy of the mantle region where the reactions occur.

Lack of isotopically light carbon in ferropericlase-bearing diamonds

Carbon isotope measurements of lithospheric diamonds demonstrate that the peridotitic suite of diamonds has strong mode with a narrow range of carbon isotopic compositions around the mantle value of $\delta^{13}C = -5 \pm 2‰$ (*55*). Values $\leq -10‰$ in $\delta^{13}C$ are scarce for peridotitic diamonds. The eclogitic and websteritic suites contain a significant population of diamonds with $\delta^{13}C \leq -10‰$ tailing down to −40‰ (*43*). The ^{13}C-depleted signature of nonperidotitic

lithospheric diamonds has typically been attributed to subducted organic carbon (*56*) or carbonates derived by its oxidation in altered oceanic crust (*52*). The carbon isotope database for sublithospheric diamonds shows that the signature of light carbon seen at localities such as Jagersfontein, Koffiefontein, and Juína (*43*) occurs chiefly in diamonds that have inclusions of majoritic garnet and Ti-rich former Ca-perovskite with compositions linking them to basaltic oceanic crust, which therefore also derive principally from organic carbon in oceanic crust subducted to the deep upper mantle and transition zone [e.g., (*15*)].

The newly measured carbon isotope compositions of the 12 Juína diamonds with ferropericlase or magnesiowüstite inclusions in this study all have restricted, mantle-like carbon isotope compositions (with a range in $\delta^{13}C$ between −5.70 and −4.39 ‰; table S3). A narrow compositional range around mantle-like values for the host diamond applies to the global ferropericlase inclusion dataset (Figs. 4 and 5), as previously discussed in (*57*).

The dominance of mantle-like carbon with little evidence of light carbon in ferropericlase-bearing diamonds (Fig. 4) is consistent with the protolith providing the diamond-forming melts being the lithospheric mantle portion of the slab, which has low surface organic carbon (*43*). In addition, diamonds that are thought to have been derived from surficial carbon usually show internal heterogeneity in isotopic composition (*58*), which is unlikely the case in our sample set based on duplicate analyses of one diamond.

This indication that the diamonds crystallized from slab mantle–derived fluids is supported by the ferropericlase compositions, which have the low-Na and -Al contents expected from a low-Na and -Al protolith such as the slab mantle (*41*). The high Mg#s of coexisting ferropericlase and bridgmanite inclusions also indicate a melt-depleted source consistent with harzburgitic slab mantle (*42*). In addition, there is an absence of inclusions with an oceanic crustal affinity, including Ca-rich majoritic-garnet, Al- and/or Ti-rich bridgmanite, and NAL and CF phases in diamonds containing ferropericlase inclusions. Typically, if diamond-forming fluids are derived from eclogitic protoliths (*13*, *21*, *26*) of the slab crust, these minerals would be present, as in the Juína-5 and Collier 4 suites with light carbon isotopic compositions (*26*). Majorite garnet is the second most common inclusion in sublithospheric diamonds after ferropericlase, yet these two types of inclusions have not been observed to co-occur within the same diamond (*41*). We also note that measured trace element abundances in ferropericlase inclusions show relative enrichments in some incompatible lithophile elements (e.g., Th, U, Nb, and Ta) suggestive of equilibration with a fluid/melt phase, and marked depletions in Y that may indicate a distinct source (*41*).

Two suites of ferropericlase inclusions and the diamond substrate

Compositionally, the entire ferropericlase dataset can be split into two groups. The first group includes Kankan and Juína samples that have high-Mg# (i.e., >0.78) and mantle-like Fe isotopic compositions ($\delta^{56}Fe = 0.00 \pm 0.10$‰; 2 SD; $n = 7$; Fig. 2) that all fall within the mantle range defined by peridotites (*59*, *60*). The second group includes low-Mg# (i.e., <0.78) ferropericlase inclusions with Fe isotopic compositions that, except for one inclusion (JH12A1, $\delta^{56}Fe = -0.23$‰), are overlapping but range to heavier than the mantle ($\delta^{56}Fe = -0.013$ to +0.24‰). The low-Mg# ferropericlase inclusions account for most of the Fe isotope variability

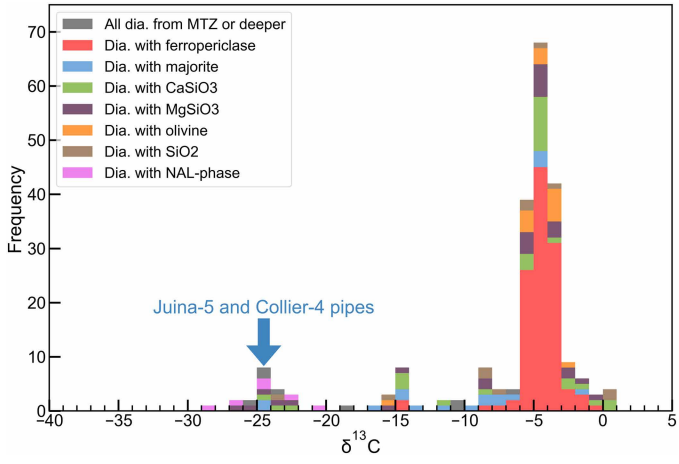

Fig. 4. Diamond carbon isotope composition classified on the basis of inclusion phases. Ferropericlase-bearing sublithospheric diamonds from the mantle transition zone (MTZ) or the lower mantle have dominantly mantle-like carbon isotope composition, including the 14 Juína diamonds analyzed in this study. Diamonds from this depth range with $\delta^{13}C$ near −25‰ are limited to the Juína-5 and Collier-4 occurrences in the Juína region of Brazil. These diamonds do not contain ferropericlase inclusions but are characterized by NAL-phase inclusions. Compiled carbon isotope dataset is from (*32*).

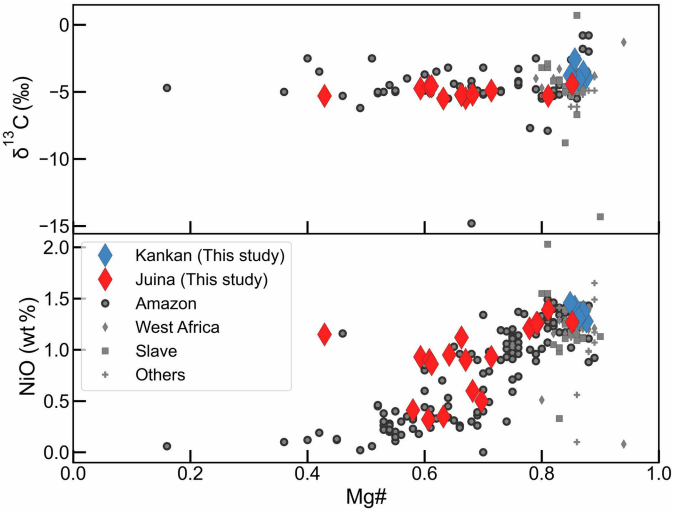

Fig. 5. Diamond carbon isotope composition (top) and NiO versus Mg# (Mg/[Mg + Fe^{2+}]) (bottom) of ferropericlase inclusions. The Kankan diamonds are slightly high in $\delta^{13}C$ value, while the Juína ones measured in this study are mostly mantle-like in carbon isotope composition. This conclusion is generally true when considering the compiled dataset from the literature. Note that the low-Mg ferropericlase inclusions are exclusively from the Amazonian craton. Compiled data are from (*41*, *43*).

in the dataset but show no obvious correlation between $\delta^{56}Fe$ and Mg# (Fig. 6).

The crystallographic orientation relationship (COR) with the diamond also allows the ferropericlase inclusion samples set to be split into two groups. A recent study of Juína and Kankan diamonds (*61*) showed that of 57 ferropericlase inclusions in 37 diamonds, 32 ferropericlase inclusions with Mg# > 0.70 had a COR

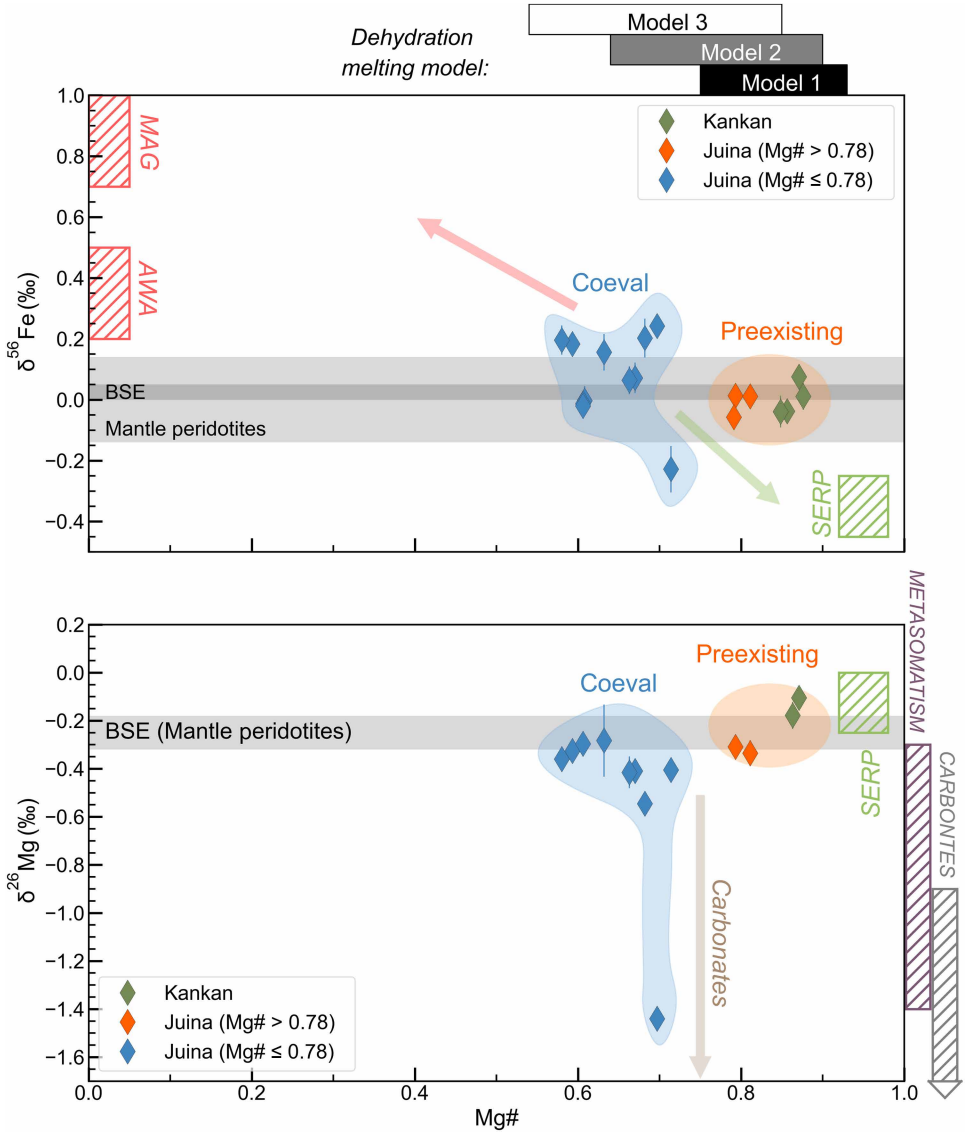

Fig. 6. Iron (top) and magnesium (bottom) isotope compositions versus Mg# of ferropericlase inclusions. Error bars represent 2 SEM. The high-Mg# ferropericlase inclusions show a limited range of Fe and Mg isotope compositions close to those defined by mantle peridotites. The low-Mg# ferropericlases, on the other hand, show much larger variations in both isotope systems that indicate contributions by additional components. The coeval and preexisting model for low-Mg and high-Mg ferropericlases, respectively, is based on the crystal orientation relationship between the ferropericlase inclusions and host diamonds (*61*). Data sources for mantle peridotites, BSE, serpentine (SERP), mantle metasomatism phases, carbonates, magnetite (MAG), and awaruite (AWA) are provided in Figs. 2 and 3. Note that these low-temperature phases are used to represent components of the slab mantle with heterogeneous Fe and Mg isotope compositions, owing to the absence of data on subducted serpentinized peridotites. The predicted Mg# ranges for ferropericlase precipitated from the dehydration melting and crystallization models (see Supplementary text) are plotted at the top of the figure for comparison with the data.

that was random relative to the diamond lattice, whereas all 25 of the ferropericlase inclusions with Mg# < 0.70 had a specific COR relative to the diamond lattice. Lorenzon *et al.* (*61*) suggested that the high-Mg ferropericlases are protogenetic (e.g., crystallized before the diamond encapsulated them) and the low-Mg ferropericlases are syngenetic (e.g., cocrystallized or coeval with their host diamonds) and therefore two genetically distinct generations of ferropericlases exist in Juína and Kankan diamonds. A theoretical follow-up study with no new analyses pointed out the technical possibility of ferropericlase inclusions with a specific COR being also protogenetic, but no direct evidence has been identified yet to support this hypothesis (*62*). Because of the different interpretations of preferred COR between low-Mg# ferropericlase inclusions and their host diamonds, we simply note that they are perhaps indicative of different formation mechanism for them compared to the high-Mg# ferropericlase. Hereafter, we will refer to these inclusions as "coeval" instead of "syngenetic" and the "protogenetic" ones as "preexisting" based on COR relationship.

We were able to obtain four released ferropericlase grains from the Lorenzon *et al.* (*61*) study—two from the population with random COR and two from the population with specific COR. The two ferropericlases that had random COR have mantle-like Fe isotope

compositions, whereas the two ferropericlase that had specific COR have slightly heavier Fe isotopic compositions. While most of our isotopic analyses are from ferropericlase inclusions with undetermined COR, we interpret the four with known COR to be representative of their respective populations. Thus, we have classified the high-Mg# ferropericlase as preexisting and the lower Mg# ferropericlase as coeval (Fig. 6 and Table 1).

The mantle-like Fe isotope compositions for the ferropericlase inclusions in Kankan diamonds, along with their high Mg# (0.85 to 0.88), the $\delta^{13}C$ of the host diamonds (−2.6 to −3.9‰; discussed above), and recent oxygen isotope measurements of enstatite inclusions in the same suite of diamonds ($\delta^{18}O$ = +5.3 to +5.8‰) (*49*), are all consistent with the inferences from the ferropericlase compositions (e.g., low Na and Al content) and lack of crustal inclusions (e.g., majorite) that the diamonds grew in meta-peridotite [or "kankanite," (*13*)] from the slab mantle not significantly mixed with recycled crustal material. The group of Juína diamonds containing high-Mg# ferropericlase inclusions appears to be equivalent to the Kankan suite in terms of their Mg# and Fe isotopic composition. In addition, the carbon isotope compositions of the host diamonds indicate derivation from a similar protolith. A preexisting origin for high-Mg# ferropericlase inclusions also supports their mantle-like Fe isotope compositions measured in this study because they would have been part of the equilibrium mineral assemblage in the mantle portion of the slab before incorporation into their host diamonds.

Juína diamonds containing ferropericlase with low Mg# appear to have a different origin. Because they are coeval in COR relation with the host diamonds, the low-Mg# ferropericlases might have precipitated at the time of diamond formation. Thus, they are likely to have tracked the Fe isotope composition of a fluid or melt phase as it left its source, reacted with host rocks, and crystallized diamonds.

Isotopically light Mg—Linkage to subducted carbonates and slab metasomatism

The Mg isotope measurements of the ferropericlase inclusions show a split between the high and low-Mg# ferropericlase inclusions, similar to the division observed in the Fe isotope data. Measured $\delta^{26}Mg$ values of the two ferropericlase inclusions from Kankan diamonds were −0.11 ± 0.03‰ and −0.18 ± 0.05‰ (2 SE), which are slightly heavier than the mantle value (−0.25 ± 0.07‰) (*5*). The two high-Mg# ferropericlases measured in Juína diamonds are both within error of the mantle $\delta^{26}Mg$ value (−0.31 ± 0.02‰ and −0.34 ± 0.05‰). The low-Mg# ferropericlase from Juína, on the other hand, demonstrates a much larger range of magnesium isotope compositions, extending toward more ^{26}Mg-depleted than the mantle composition ($\delta^{26}Mg$ = −1.44 ± 0.04‰ to −0.29 ± 0.14‰), with an average $\delta^{26}Mg$ value of −0.48 ± 0.70‰ (2 SD). The large variance about the mean is largely due to one ferropericlase (BZ70) with an extreme $\delta^{26}Mg$ value of −1.44 ± 0.04‰. Even when this sample is excluded, all low-Mg# ferropericlase inclusions from Juína lie exclusively to the lower side of the bulk silicate Earth composition ($\delta^{26}Mg$ = −0.25 ± 0.07‰, 2 SD) (*44*).

The offset in magnesium isotope composition to slightly heavier than mantle values for the two Kankan ferropericlase inclusions would be in concert with the slightly heavier Mg isotopic composition seen for serpentinite ($\delta^{26}Mg$ = averaged −0.14‰) (Fig. 2). However, the possibility that ferropericlase directly inherit light Mg from a serpentinite precursor is low because of the lack of the extremely light Fe isotope signature of serpentinite ($\delta^{56}Fe$ ~ −0.4‰) in these ferropericlases (average $\delta^{56}Fe$ = 0.0‰; Figs. 2 and 6). The preexisting COR with diamond suggests that the ferropericlase incorporated in the diamond was from the ferropericlase and bridgmanite assemblage formed by the decomposition of ringwoodite. Fractionation factors between ferropericlase and bridgmanite have not been determined. Nonetheless, if existing equilibrium isotope fractionation data (fig. S2) with coexisting silicates such as olivine or pyroxene at 1100° to 1200°C can be used as a guide, ferropericlase is expected to be 0.1 to 0.2‰ heavier than the bulk mantle.

The lower $\delta^{26}Mg$ values of up to −1.44‰ for the low-Mg# ferropericlase inclusions in Juína diamonds cannot be explained by equilibrium fractionation processes commonly occurring in the silicate mantle. Mantle partial melting and magmatic differentiation in the upper mantle are known to have limited effects on magnesium isotope fractionation, as evidenced from the highly consistent Mg isotope compositions of mantle peridotites, MORBs, and OIBs (Fig. 3). Teng *et al.* (*44*) reported an average Mg isotope composition of $\delta^{26}Mg$ = −0.25 ± 0.04‰ (2 SD) for mantle peridotites,

Table 1. Summary of geochemical and mineralogical information of sublithospheric diamonds from Kankan (Guinea) and Juína (Brazil) in this study and from literature. Diamonds are grouped on the basis of the type of (or absence of) ferropericlase inclusions they contain. Iron and Magnesium isotope data are from this study. Carbon isotope data are from this study and literature (*43*). Oxygen isotope data are from (*125*). Crystal orientation analyses were reported in (*61*). Mineral inclusion information is from the compiled dataset in (*41*).

Diamond group	High-Mg fpr (Kankan)	High-Mg fpr (Juína)	Low-Mg fpr (Juína)	Fpr-free (Juína)
# of diamonds	~42	~59	~95	~33
$\delta^{56}Fe$	Mantle-like	Mantle-like	More variable, often heavy	N/A
$\delta^{26}Mg$	Mantle-like (slightly heavy)	Mantle-like	More variable, often light	N/A
$\delta^{13}C$	Averaged −4‰	Averaged −5‰	Averaged −5‰	Clear mode of −25‰
$\delta^{18}O$	Mantle-like	N/A	N/A	Heavy
Crystal orientation	N/A	Preexisting	Coeval	N/A
Coexisting mineral inclusions	CaPv* (3) MgPv† (5)	CaPv (2) MgPv (14) Jeffbenite (5)	CaPv (2) MgPv (3) Jeffbenite (0)	High-Al MgPv (4) High-Ti CaPv (8) NAL-phase (6)

*Retrograded Ca-perovskite inclusion †Retrograded Mg-perovskite inclusion

−0.24 ± 0.06‰ for global MOBRs, and −0.26 ± 0.08‰ for OIBs, which are within uncertainty from each other and show a limited range. More recent data expanded the magnesium isotope range to as low as −0.4‰ for some OIBs, whose low δ^{26}Mg values have mainly been attributed to pyroxenite melting (*63*) and diffusive Fe-Mg exchange (*64*).

The light Mg isotope enrichment is also unlikely to be caused by kinetic processes because diffusion-limited or reaction rate–limited growth of the inclusions would also affect the Fe isotopes by enriching the lighter isotope (^{54}Fe) in these same ferropericlase inclusions, which is not observed (Figs. 2 and 6). More likely, the light Mg isotopic signature in these ferropericlase grains is derived from other components in the altered slab mantle that were produced by relatively low-temperature processes on or near the ocean floor.

Serpentinites are a major carrier of Mg in the subducted slab mantle, but they are slightly enriched in ^{26}Mg (δ^{26}Mg = −0.14‰ on average) (Fig. 2) due to seawater-silicate equilibrium during hydrothermal circulation and serpentine crystallization. This compositional difference is opposite to the light Mg isotope composition (lower ^{26}Mg/^{24}Mg ratios) observed for the low-Mg# ferropericlase. Although seawater has a homogeneous, isotopically light Mg composition partly due to serpentinization (*54*, *65*), seawater is lost at shallow levels during subduction. The only mechanism to carry water to great depths is by the hydroxyl molecule in serpentine and eventually as a substitutional component in dense hydrous magnesium silicates (*48*, *49*).

Carbonates are known to have weak bond strengths relative to silicates and therefore tend to be enriched in the lighter isotope of Mg (*66*). Biogenic and abiogenic carbonates, for example, show large ranges of ^{26}Mg-depleted compositions with calcite-rich carbonates ranging from −5.57 to −1.04‰ and dolomite-rich ones ranging from −3.25 to −0.38‰ in all types of terrestrial rocks (*54*). The enrichment of light isotopes of Mg in carbonates is not only reflected in sediments but also seen in altered oceanic crust (*65*). Subduction of carbonate-bearing altered oceanic crust and marine sediments is commonly thought to be the cause for light Mg enrichment in cratonic eclogites (*67*–*69*), continental basalts (*70*–*72*), and metasomatized mantle xenoliths (*73*, *74*). The presence of carbonates in serpentinized peridotites is also supported by a recent study of the Lost City hydrothermal field on the Atlantis Massif (*75*, *76*), which documented the mineralogy and textures of carbonates distributed throughout serpentinized peridotites.

The light Mg isotopic composition of low-Mg# ferropericlases in Juína diamonds may indicate a contribution of subducted carbonates as the source of light Mg to the diamond-forming fluids. The possible contribution of carbonates to the formation of low-Mg# ferropericlase inclusions is further evidenced by a recent study of a separate suite of diamonds from Juína, which reported a touching pair of low-Mg# ferropericlase and magnesite inclusions (*77*).

A less common yet possible alternative source of light Mg found in the serpentinites are the Ti-clinohumite dikelets and metarodingites. Carvalho *et al.* (*78*), for example, found a hydroxylclinohumite inclusion in another suite of sublithospheric diamonds that indicates a serpentinite protolith. As plotted in Figs. 3 and 6, these Mg- and Ca- metasomatized rocks contain high amounts of MgO (>30 wt %) and could be extremely light in Mg isotopic composition (as light as −1.49‰) (*79*). Subduction of such metasomatized components associated with meta-serpentinite could potentially introduce a light noncarbonate Mg reservoir that contributed to the formation of the low-Mg ferropericlases measured in this study.

Ferropericlase formation by dehydration melting of deeply subducted slab mantle

A formation model for the studied ferropericlase suite should be able to explain the characteristics of the suite as summarized here and in Table 1: (i) the correlated and wide variation in Mg# among co-occurring bridgmanite and ferropericlase inclusions (*41*); (ii) the positive trend between NiO and Mg# in ferropericlase inclusions (Fig. 5); (iii) the preexisting and coeval COR with the host diamond; (iv) the mantle-like carbon isotope composition of the host diamonds; and (v) the systematic differences in Fe and Mg isotope compositions of the ferropericlase.

Formation of ferropericlase-bearing sublithospheric diamonds has been attributed to several possible mechanisms: the melting of carbonated oceanic crust (*29*), the general reduction of slab-released carbon-bearing fluids/melts, or the partial decarbonation of ferromagnesite (*50*). Any one of these mechanisms could be part of explaining the crystallization of ferropericlase at depths ranging from the upper mantle to the top of the lower mantle. The melting of carbonated oceanic crust, for example, is especially germane to the majorite-bearing, isotopically light carbon–enriched diamonds that indicate a parental lithology of subducted oceanic crust (Table 1). As we noted above, however, none of these majorite-bearing diamonds also contain ferropericlase inclusions. However, a solely crustal protolith does not have the composition needed to explain the collective geochemical characteristics seen in the ferropericlase-bearing diamonds studied here and ferropericlases in the literature that are similar to our suite.

Here, we propose a petrological model for producing ferropericlase-bearing diamonds at the top of the lower mantle that takes into account diamond and ferropericlase isotopic composition, ferropericlase major and trace element composition, and crystallography. The model, as depicted schematically in Fig. 7, incorporates the types of alteration [e.g., serpentinization and carbonate veining; (*75*, *80*, *81*)] that have been observed to affect the slab mantle before subduction. It is also partly inspired by recent high pressure experiments indicating that hydrous melting at lower mantle pressures can occur at relatively low temperatures (*82*–*84*). This model is potentially capable of explaining the geochemical and crystallographic characteristics of the ferropericlase inclusions as summarized in Table 1. We emphasize, however, that further experiments are needed to investigate the petrological and geochemical details of this scenario and to better constrain its relation to existing ideas on ferropericlase formation.

The model assumes a parental lithology of partially serpentinized slab mantle for the ferropericlase-bearing diamonds because serpentinizition is a common feature produced by seawater alteration before and during early stages of subduction (*75*, *76*, *85*–*90*). Hydrothermal circulation of seawater through the slab mantle creates stockworks of fluid altered rock and serpentinite surrounded by and adjacent to unaltered harzburgitic mantle. These juxtaposed lithologies exhibit strong contrasts in oxidation state and degree of hydration. We propose that upon subduction to the top of the lower mantle, the redox differences and hydration gradients between them become essential factors in sublithospheric diamond formation (*91*).

During subduction of older and colder slabs, serpentinized slab mantle can avoid shallow dehydration affecting warm and young

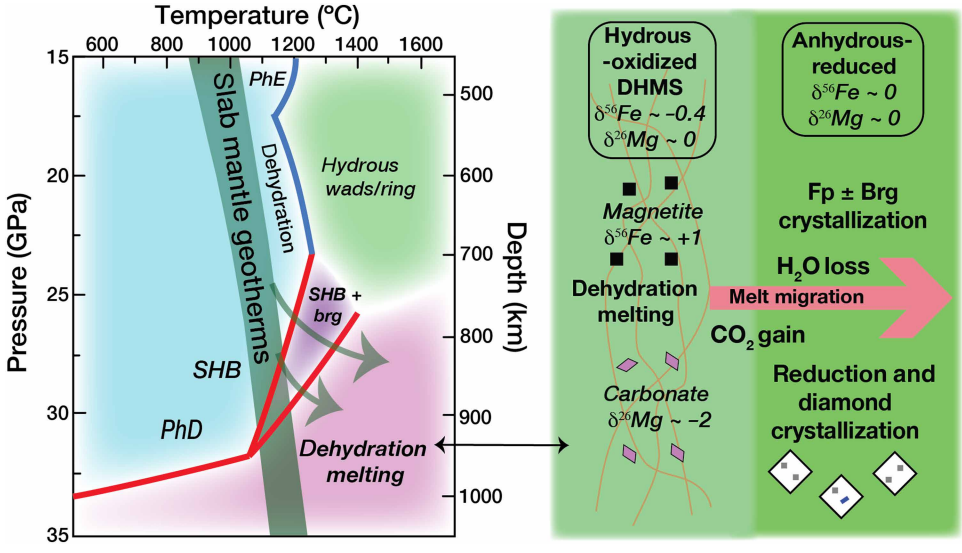

Fig. 7. Schematic diagram illustrating the model of dehydration melting and ferropericlase crystallization. Isotopic compositions are relative to mantle values in per mil unit. Phase diagram for hydrous slab mantle is modified from (*40*), licensed under CC BY 4.0 (http://creativecommons.org/licenses/by/4.0/). Changes including pressure-temperature range adjustment and restyling. Hydrated regions of cooler slabs depicted in the left diagram may transport as much as 5 wt % water in hydrous phases deeper into the mantle. When heated up in the shallow lower mantle, the hydrated portions of the slab will undergo dehydration melting due to the breakdown of phase D or superhydrous phase B, producing an H_2O-rich partial melt. As illustrated on the right diagram, this hydrous and oxidized melt generated in the serpentinized regions of slab mantle (i.e., "alphabetite") will migrate into the anhydrous and reduced slab mantle harzburgite (i.e., kankanite) due to their low density and viscosity (see Supplementary Text). Loss of H_2O to the anhydrous surrounding promotes crystallization of ferropericlase ± bridgmanite. The isotopic composition of the initial hydrous melts may take on values close to the mantle values, but migrating melts can sample magnetite or iron melt with highly positive δ^{56}Fe values and/or carbonates with highly negative δ^{26}Mg, yielding the idiosyncratic variation in these isotope systems observed in the coeval ferropericlase inclusions. Carbon dioxide dissolved in the hydrous melt is reduced to diamond due to the strong redox gradient between the oxidized melt and reduced slab mantle. SHB, superhydrous phase B; PhD, phase D; PhE, phase E; brg, bridgmanite; fp, ferropericlase.

slabs by converting serpentine into dense hydrous magnesium silicates, such as phase A and phase E (Fig. 7) (*14*). After reaching the transition zone and/or lower mantle depths, subducted slab can stagnate at the top of the lower mantle because of its lower density. There, it would warm up over time and undergo hydrous melting from the serpentinized portion of the slab mantle (*14*) because of its considerably lower solidus. On the basis of recent experiments, this melting process can happen at temperatures below 1300°C and produce a water-rich melt with ~40% H_2O (*82*). With a lower density than the surrounding slab mantle and a low viscosity (*92*), this hydrous melt is expected to migrate upward from its source region and react with more reducing, dry harzburgitic portions of the subducted slab mantle [also referred to as kankanite; (*59*)]. During migration, the melt will lose some of its H_2O to anhydrous minerals (e.g., bridgmanite and ferropericlase) and become reduced, leading to crystallization of ferropericlase ± bridgmanite along with diamonds (Fig. 7).

A more detailed discussion of the model is included in Supplementary Text to demonstrate the feasibility of the melt infiltration process and consequent reactions leading to ferropericlase ± bridgmanite crystallization. This model can produce two populations of ferropericlase inclusion in diamonds. Existing high-Mg# ferropericlase formed as part of the high-pressure assemblage in the dry harzburgitic portion of the slab mantle can be trapped in the diamond hosts, becoming preexisting inclusions in diamonds. Ferropericlase precipitated from the hydrous melt, however, will be coeval with the diamond hosts because they formed simultaneously during melt infiltration (Fig. 7). Our model shows that this population of ferropericlase becomes progressively Fe-rich in composition as the melt evolves, which correlates with Mg# of crystallized bridgmanite. Using Fe-Mg exchange coefficients and Ni partition coefficient from the literature (*83*, *93*), our model also successfully reproduces the observed correlations between Mg# of bridgmanite and ferropericlase inclusions, and Ni concentration and Mg# of ferropericlase (Supplementary Text).

An essential geological aspect of ferropericlase crystallization is that each inclusion has been encapsulated from one individual diamond whose crystallization occurred from its own little hydrous melt—host rock system. The studied ferropericlase population from 17 diamonds is not necessarily a product of one batch of melt but rather 17 batches of melt derived each from their own sources with similar but not identical modal mineralogy. We do not expect good elemental abundance and isotopic correlations with Mg number of ferropericlase but simply that they equilibrate with variable amounts of similar phases in the slab.

The preexisting ferropericlase inclusions formed in the above model would inherit geochemical characteristics of the original depleted harzburgite and have high Mg# and high Ni contents, and be similar to the mantle in δ^{26}Mg, δ^{56}Fe, δ^{13}C, and δ^{18}O compositions that match the observations summarized in Table 1. For the coeval ferropericlase inclusions, the mantle-like carbon isotope compositions of the host diamonds agree with a parental lithology of serpentinized slab mantle with little organic carbon. Their more variable Fe and Mg isotope composition of the ferropericlase inclusions can be explained by the uneven incorporation of Fe-bearing and Mg-bearing phases that are variable in isotopic composition when

initially formed during serpentinization or metasomatism, such as magnetite, native iron alloys, Fe-rich or Mg-rich carbonates, titanoclinohumites, or meta-rodingites (Figs. 3, 4, and 6). Incorporating these phases disproportionally during migration of the hydrous melt can explain the more variable Fe–Mg isotope systematics of the low-Mg#, coeval ferropericlase inclusions (Fig. 7, also see Supplementary Text for more detailed discussions).

A simple mass balance mixing calculation shows that, for a hydrous melt with ~30 wt % MgO and a serpentinite-like δ^{26}Mg of 0‰, and a carbonate with ~30 wt % MgO (e.g., magnesite) and δ^{26}Mg of −2‰, most of the measured ferropericlase inclusions would require an ~90:10 ratio of melt to carbonate. For the ferropericlase inclusion with the lowest δ^{26}Mg value of −1.4‰, the mixing ratio would be ~30:70. A hydrous melt percolating through altered slab mantle may incorporate a substantial carbonate component and become locally more carbonatitic (Fig. 7). Notably, the diamonds themselves attest to a carbon-saturated melt and may reflect preferential sampling of those melts that interacted most extensively with carbonate in the altered mantle.

Ferropericlase and the onset of melting of subducted cold slab mantle

A recent geochronologic study (*39*) of breyite (retrogressed Ca-silicate perovskite) inclusions in Juína and Kankan diamonds helps to constrain the timing and geologic setting of the slab melting that produced ferropericlase. Not only are the dated diamonds from the same Juina and Kankan localities, but Ca-silicate perovskite inclusions suggest that these diamonds were also derived from the slab mantle at lower mantle depths (*39*). Furthermore, about half of the dated diamonds have ferropericlase inclusions (*39*). The Juína and Kankan diamonds crystallized around 450 to 650 million years ago, when the Amazonian and West African cratonic nuclei were assembled together as the interior of the Gondwana supercontinent (*39*). Timmerman *et al.* (*39*) proposed that subduction around the edge of Gondwana transported altered, cold oceanic slab mantle into the lower mantle below the supercontinent. There, during heating and devolatilization, diamonds were formed from the expelled fluid/melt and subsequently transported upward together with the depleted buoyant mantle residues in the parts of the slab where they were generated. Our detailed stable isotopic compositions for C, Fe, and Mg on diamonds and their preexisting and coeval ferropericlase inclusions, which span a large range in Mg#, suggest how the slab began to melt and produce diamond-forming fluids/melts.

The hydrous melt infiltration and bridgmanite ± ferropericlase crystallization model discussed above and in Supplementary Text involves rocks wholly within the slab mantle. These different rock types would be physically in proximity and their interaction would not have involved the slab crust, whose melting should have already occurred separately in space and time from the melting of the slab mantle. The slab crust heats up faster, dehydrates in the upper mantle (e.g., <300 km), and has a lower solidus temperature compared with the slab mantle. Therefore, by the time slab mantle has heated up sufficiently to undergo dehydration melting in the lower mantle, CO_2-bearing crust should have already partially melted in the deep upper mantle or transition zone, leading to diamond formation through redox freezing and crystallization and trapping of Ca-rich majorite and Ca silicate perovskite inclusions (*28*, *40*, *41*, *53*). In addition, the density contrast between the meta-basaltic slab crust and the underlying slab mantle may trigger delamination during subduction, perhaps physically separating them even before the slab reaches the top of the lower mantle (*94*, *95*). Thus, the diamond forming fluids causing the encapsulation of the ferropericlases avoid incorporating much isotopically light carbon as seen in other crustally derived Juína diamond suites that originated in the upper mantle and transition zone [e.g., (*22*)]. The hydrous melt infiltration model also provides a mechanism that physically separates rock fragments from the slab mantle along the preexisting serpentinization network, allowing these lower-density rocks to be entrained by upwelling mantle convection and brought up to the upper mantle rather than subducted further into the lower mantle as heating and complete phase transition occur for the slab.

While the Juína and Kankan diamonds are linked by their ages and thus the subduction system around Gondwana, the localities are separated by many hundreds of kilometers along the strike of the slab. The physical distance means that they are not produced from a single, spatially related occurrence of evolving melt/fluid in a portion of the same slab mantle. Therefore, compositional differences and different evolution paths are expected for ferropericlase and diamonds at each locality. Specifically, the Kankan suite of diamonds has ferropericlase with a slightly higher Mg# and a more restricted Mg# range compared with the Juína suite. Further differences between the suites could also arise from sampling bias by the kimberlitic magma that extracted these diamonds from the supercontinent's mantle keel.

Differences between the Kankan and Juina ferropericlase inclusion suites might also reflect original differences in the extent of alteration when the oceanic lithosphere was first created, perhaps due to the well-known relationship between spreading rate differences and degree of serpentinization (*96*). For example, the degree of depletion and serpentinization depends greatly on the depth of melt detachment beneath the slab surface (*97*) and spreading rate [e.g., (*75*, *76*)].The outer rise, just before subduction, is another region where oceanic lithospheric mantle can be serpentinized along deep-seated fracture systems formed by bending (*80*, *81*). Here, large contrasts in the degree of serpentinization could also occur, but the detailed differences are less predictable. Nonetheless, it is evident that the oceanic lithosphere will be subducted with heterogeneity created by differences in degree of seawater alteration and serpentinization on a variety of scales. These features are inherent to any section of hydrothermally altered slab lithosphere, and we suspect that they may be critical in understanding differences in separate diamond suites. We speculate here that the Kankan ferropericlase inclusions could have been derived from slab mantle created by a moderately serpentinized ridge mantle, whereas Juína ferropericlase inclusions could have been derived from a slab mantle segment that experienced more extensive serpentinization and carbonatization. Thus, sublithospheric diamonds with oxide inclusions, like their metallic counterparts (*53*, *98*), bear direct witness to surficial processes occurring during creation of the oceanic lithosphere.

MATERIALS AND METHODS

Diamond samples and ferropericlase inclusions

The 19 ferropericlase inclusions analyzed in this study were hosted in 19 individual diamonds recovered from the Kankan district of Guinea and the Juína region of Brazil. Ferropericlase inclusions in Kankan diamonds come from the diamond suites studied by Stachel (*30*–*32*) that were purchased in the provincial capital of Kankan

(*30*). They were obtained as released, isolated grains from previously studied diamonds. Ferropericlase inclusions from the Juína region of Brazil come from type II diamonds purchased on collecting trips to the town of Juína in 2014 and 2019, as well as samples previously reported on by Harte and coworkers (*18*, *34*). The five diamonds from Kankan are colorless and octahedral or dodecahedral in shape. They contained ferropericlase inclusions that are approximately 100 to 300 μm in diameter. Two of the five diamonds contained more than one ferropericlase inclusion, but only the largest in each diamond was used for isotopic analysis. Besides ferropericlase, additional inclusions of $MgSiO_3$, olivine, and siderite were also present in these diamonds (*31*). The diamonds from Juína region of Brazil are colorless to pale yellow/brown in color and are irregular in shape. Most of them contained one to three ferropericlase inclusions that are optically visible, but some specimens contained clusters of small ferropericlase inclusions that are tens of micrometers in diameter (e.g., 6b05 and N5a). The ferropericlase inclusions in Juína diamonds are dark in color, flat, elongated, or rounded in shape. Some of them show the characteristic peacock color when in diamond. Those selected for isotopic analysis are typically 100 to 300 μm along the longest dimension. Raman analyses of silicate phases in 6b05 from Juína confirmed the presence of olivine and retrograded $CaSiO_3$ phases (walstromite and larnite), supporting the sublithospheric depth of origin (fig. S4). In eight of the Juína diamonds (table S2), previous synchrotron x-ray diffraction analyses identified grains of titanomagnetite and olivine (*99*).

Inclusion exposure and dissolution

The 5 ferropericlase inclusions from Kankan and 8 of the 14 from Juína were previously exposed by cracking the host diamonds and have been polished on one side for electron microprobe analysis (*17*, *31*, *61*, *100*). These inclusions have been kept either on a piece of clear tape or in epoxy resin mounts before this study. Inclusions on the tape were carefully moved to individual polytetrafluoroethylene (PTFE) vials using a pair of plastic tweezers for dissolution. Inclusions mounted on epoxy resin were dug out by a tungsten carbide drill bit and moved to PTFE vials for dissolution. Before sample dissolution, the inclusions were cleaned repeatedly with acetone and ethanol to remove residual organic compounds from the tape and the epoxy mount. After cleaning, each of the inclusions was moved into a brand-new PTFE vial and the inclusions were dissolved in 0.6 to 0.9 ml of mixed concentrated HCl and HNO_3 at 120°C for at least 48 hours.

The other six inclusions from Juína were first isolated into smaller diamond fragments from their hosts by a laser cutting instrument. The diamond fragments containing the target ferropericlase inclusions were subsequently polished using conventional diamond polishing methods on a scaife to expose the inclusions. When preparing for sample dissolution, the diamond surface was cleaned with distilled acetone and ethanol to remove organic contaminants. The exposed inclusion surface was protected with a small drop of crystal bond, and then the diamond fragment was placed in a Teflon vial and soaked in 0.4 to 1 ml of 6 M HCl at room temperature for 3 to 21 days to further clean the surface following a procedure previously reported in (*53*). The cleaning hydrochloric acid in the vial was replaced every 1 to 4 days and measured for Fe and Mg contents to track the surface blanks of Fe and Mg.

Composition of the leachates were analyzed using an iCapQ quadrupole inductively coupled plasma mass spectrometry (ICP-MS) to measure the amount of Mg and Fe yielded by each step of leaching. The first leachates of the diamond fragments contained 40 to 1000 ng of Fe and 20 to 100 ng of Mg. Within the 3 to 21 days of cleaning, the Fe and Mg contents of the leachates both decreased to 1 to 4 ng, insignificant comparing to the 100 to 1000 ng of Fe and Mg yielded by the inclusions (table S4). After being cleaned in 6 M HCl, the crystal bond on the diamond surface was removed by distilled acetone and distilled ethanol. The diamond fragment was then moved to a virgin Teflon beaker, and the exposed inclusion was dissolved out of the diamond using 0.4 ml of 6 M HCl at room temperature for at least 48 hours. The diamond was examined under a binocular scope throughout the process to make sure that the inclusion remained intact during cleaning and completely extracted during dissolution (fig. S5). Dissolution of the ferropericlase was tested in advance using a synthetic ferropericlase (SynFpr, $Mg_{0.82}Fe_{0.18}O$) powder, and complete dissolution was achieved overnight at 110°C with either 6 M HCl, concentrated HNO_3, or 2:1 HCl:HNO_3.

Carbon isotope analysis

Carbon isotope measurements were conducted on 12 diamonds from Juína with ferropericlase or magnesiowüstite inclusions at Carnegie Institution for Science. Diamond fragments, weighing between 0.25 and 1.5 mg, were obtained either by laser cutting or through mechanical inclusion release from previously cut diamond wafers. Each fragment was placed in a platinum crucible and inductively combusted at 1500°C in analytical grade oxygen (0.5 bar). The combustion process lasted up to 4 min and was monitored by a pressure gauge.

The resulting CO_2 was frozen in a one-fourth–inch (~0.64 cm) Pyrex glass finger attached to the vacuum line and submerged in liquid nitrogen, with residual oxygen being pumped away after all CO_2 was frozen. The glass finger was then flame-sealed and loaded into a Swagelok tube cracking device. By cracking the glass tube under vacuum, the CO_2 was introduced into the dual-inlet system of a Thermo Finnigan Delta Plus XL isotope ratio mass spectrometer and measured against an in-house CO_2 reference gas. External referencing was performed using USGS24 (Graphite, $\delta^{13}C_{VPDB} = -16.05$ ‰), treated similarly to a diamond sample. The reproducibility of the combustion method is 0.05 ‰ (1 SD) based on USGS24 ($n = 8$).

Raman spectroscopy

Raman imaging was conducted using a WITec confocal Raman microscope system at the Earth and Planets Laboratory of Carnegie Institution for Science. A frequency-doubled solid-state yttrium aluminum garnet laser was operated at 532 nm with an output power of ~1 mW as the source. The system used a long working distance objective and a 50-μm optical fiber as the confocal pinhole. Raman spectra were collected using an f/4 diafragma 300-mm focal length imaging spectrometer and a Peltier-cooled Andor electron multiplying charge-coupled device camera for signal collection. After data collection, the combined image file was cosmic ray reduced, baseline corrected, and analyzed for phases using the Witec Project 5 software.

Electron microprobe analysis

Before dissolution, major (MgO and FeO) and trace element (Na_2O, SiO_2, Al_2O_3, Cr_2O_3, NiO, and MnO) compositions of the ferropericlase inclusions were analyzed using a JEOL 8530 F field-emission sourced electron microprobe at the Earth and Planets Laboratory of

Carnegie Institution for Science. Beam conditions of 15 kV, 15 nA, and 5 μm were used for all analyses with 30 s of counting time for all elements. Standardization was conducted using DJ35 for Na and Si, pure oxides for Al, Mg, and Mn, chromite for Cr, magnetite for Fe, and Ni-olivine for Ni. Each inclusion was analyzed 8 to 12 times depending on the size of the exposed area of the inclusion. Analyses hitting fractures or the boundary of the inclusion yielding low totals were excluded from the results, and the averages of the rest of the data are reported as the mean composition of the inclusion in table S1. A subset of inclusions in our study are from Harte and coworkers (*18*) and were used as secondary standards for electron microprobe analyses. The compositions obtained using our protocol are within error from published results (*34*).

Iron and magnesium isotope geochemistry

Iron column purification was conducted using one-step ion-exchange chromatography similarly to previously reported in (*53*) and briefly summarized below. The dissolved ferropericlase inclusions were converted to chloride form by drying down the solution and taken up again in a few drops of concentration HCl. The process was repeated for two to three times to drive away any nitride residue from dissolution. Heat-shrinkage Teflon columns loaded with 0.1 ml of Bio-Rad AG1-X8 resin (100 to 200 mesh) were used for separating Mg and Fe from the sample. The sample was loaded on the column in <100 μl of 6 M HCl (+ 0.001% H_2O_2) and the Mg fraction was eluted in 1.2 ml of 6 M HCl (+ 0.001% H_2O_2). The Fe fraction of the sample was subsequently eluted in 2 ml of 1 M HCl. Note that any impurities in the ferropericlase (e.g., Ni, Mn, Cr, and Na) were also collected with the Mg fraction. The Mg and Fe fractions of the sample were evaporated to dryness and dissolved in 5 μl of concentrated HNO_3 and 400 μl of concentrated H_2O_2 at 90°C overnight to react away organic compounds from the resin. The purified Mg and Fe samples were further processed with concentrated HNO_3 to remove any excess chlorine and then taken up in 1 ml of 0.4 M HNO_3 for Mg and Fe isotope analyses. The column procedure constantly gives high yields for Mg and Fe approaching 100%, as being tested by processing standards with known concentrations. A small percentage (<10%) of Fe could occasionally be lost during evaporation, but it does not cause measurable fractionation in Fe isotopes based on the tests in (*53*). To check on the reproducibility of column chemistry and isotopic measurements, a solution of the "SynFpr" was regularly processed with column chemistry and measured for Fe and Mg isotopes.

Iron isotope measurements

Isotopic compositions of the Fe fractions of the ferropericlase inclusions were measured using a Nu Plasma II MC-ICPMS at Carnegie Science following the same protocol as previously described in (*53*). Iron solutions were diluted to 250 or 500 parts per billion (ppb) using 0.4 M HNO_3 and introduced to the mass spectrometer via an Aridus III desolvating nebulizer. The concentrations of the iron solutions were selected to achieve approximately 7 to 12 V on ^{56}Fe, 0.4 to 0.7 V on ^{54}Fe, and 0.17 to 0.26 V on ^{57}Fe. Measurements were conducted with mass resolution power of >8000 to resolve $^{57}Fe^+$ and $^{56}Fe^+$ from argon-related interferences. Potential isobaric interference of $^{54}Cr^+$ on $^{54}Fe^+$ was monitored using $^{53}Cr^+$ and subtracted from $^{54}Fe^+$ signals. The monitored intensity on $^{53}Cr^+$ is usually <0.7 mV, leading to a correction of <0.2 mV on $^{54}Fe^+$, which is insignificant to cause fractionation on the results after correction as tested on isotope standards. The sensitivity was 14 to 24 V/ppm (parts per million) on ^{56}Fe, which was improved to 32 to 44 V/ppm on ^{56}Fe after an upgrade on the plasma end of the Nu Plasma II in September 2022. Each sample was analyzed 4 to 12 times, and each analysis included 20 cycles of 4-s integration. Instrument-based mass fractionation was corrected using the standard-sample bracketing technique, and the Fe isotopic compositions of the samples are reported relative to IRMM-524a, a standard that has identical Fe isotopic composition compared with the international standard IRMM-014: $\delta^{56}Fe = \left[\left(^{56/54}Fe_{Sample}\right)/\left(^{56/54}Fe_{IRMM-524a}\right) - 1\right] \times 1000‰$. Three geological reference materials (BHVO-2, BIR-1, and AGV-2) have been regularly purified using the "short-column" procedure of Craddock and Dauphas (*101*) and analyzed using the Nu Plasma II for Fe isotope composition. Measured iron isotope compositions of the three reference materials agree well with those reported in the literature (*53*, *102*). An in-house Fe concentration standard ("SPEX") was analyzed at the beginning of every mass spectrometer session to check for consistency of the Fe analysis. Repeated analyses of the SPEX in-house standard yielded a weighted mean of $\delta^{56}Fe = 0.007 \pm 0.018‰$ (2 SE, $n = 7$) over one and half years (fig. S6). In addition, solution of an SynFpr was purified together with the inclusion diamond samples, and the Fe fractions of the column were checked for consistency in the procedures. The analyses yielded a weighted mean of $\delta^{56}Fe = 0.523 \pm 0.018‰$ (2 SE, $n = 7$) over the duration of the project (fig. S7).

Magnesium isotope measurements

The Mg fractions of the ferropericlase inclusions were used for Mg isotope measurements. On the basis of the column calibration previously conducted for the work in (*53*), any impurities in the ferropericlase, such as Cr, Mn, Ni, and Na, are expected to be eluted off the column together with Mg. Electron microprobe analyses of the ferropericlase inclusions show that their trace elements are within ~5 mol % of the magnesium concentrations (table S2), which satisfies the typical criteria of matrix/Mg < 5% for successful magnesium column purification in the literature [e.g., (*44*)]. Nonetheless, the Mg fractions of the ferropericlase samples were further measured using a Thermo Fisher Scientific iCap Q quadrupole ICP-MS at Carnegie Institution for Science to check for the concentrations of matrix elements. An aliquot of the Mg fractions was diluted to contain 8- to 80-ppb Mg for analysis. A set of mixed mass spectrometer concentration standards was used for the standardization of Na, Mg, Al, K, Ca, Sc, Ti, V, Cr, Mn, Fe, Co, Ni, Cu, Zn, Sr, and Y. Among these elements measured, Sc, Cu, Zn, Rb, Sr, and Y were below detection limit most of the time. The molar concentrations of Ti, V, Co, and Ni are below 0.5, 0.3, 0.2, and 0.5% those of Mg in all samples measured. The molar concentrations of Cr and Mn are within 2% of Mg. Calcium and aluminum concentrations are within 3% of Mg except for BZ260D (Ca/Mg = 7.2) and 6b06 (Al/Mg = 7%), which are both excluded for Mg isotope analyses. The concentrations of Na and K had relatively large errors due to the high levels of background signals, leading to a detection limit of approximately 3% for Na/Mg and 2% for K/Mg. To be conservative with the level of matrix elements in the Mg samples, any samples with (Na + K)/Mg > 15% were excluded for Mg isotope analyses.

Magnesium isotope analyses were conducted in low-resolution mode using the Nu Plasma II MC-ICPMS at Carnegie Science. A small portion of the Mg fraction of the ferropericlase inclusion was diluted to 20 ppb in 0.4 M HNO_3 for analysis. The solution was

introduced into the mass spectrometer by an Aridus III desolvating nebulizer, and the sensitivity was approximately 350 V/ppm for ^{24}Mg. Instrumental mass bias was corrected by sample-standard bracketing with the signal levels matched to within 10% between sample and standard. Each sample was measured six to eight times with each analysis consisting of 20 cycles of 4-s integrations. The bracketing standard used in this study was FZT-Mg from University of Washington, which is 1.176‰ lighter in $\delta^{25}Mg$ and 2.284‰ lighter in $\delta^{26}Mg$ (pers. comm. with F.-Z. Teng) compared with the international reference material DSM-3 that is no longer available. All Mg isotope compositions are reported relative to DSM-3 after correcting for the difference between FZT-Mg and DSM-3: $\delta^{X}Mg = \left[\left(^{X/24}Mg_{Sample}\right)/\left(^{X/24}Mg_{DSM-3}\right) - 1\right] \times 1000‰$, where X is 25 or 26. The relative difference between FZT-Mg and DSM-3 was verified by analyzing a small aliquot of DSM-3 as the sample using FZT-Mg as the bracketing standard, which yielded $\delta^{25}Mg$ and $\delta^{26}Mg$ values both within analytical error from 0‰. An in-house Mg-concentration standard (SPEX) was used to check for the consistency of mass spectrometer analysis for Mg. Ten repeated analyses of the SPEX standard throughout the project time period yielded a weighted mean of $\delta^{25}Mg = -0.363 \pm 0.015‰$ (2 SE, $n = 10$) and $\delta^{26}Mg = -0.698 \pm 0.026‰$ (2 SE, $n = 10$). In addition, the magnesium fraction of the SynFpr purified together with the inclusion samples from diamond were also measured for Mg isotopes to check for consistency in the procedures. The analyses yielded a weighted mean of $\delta^{25}Mg = -0.398 \pm 0.018‰$ (2 SE, $n = 5$) and $\delta^{26}Mg = -0.763 \pm 0.030‰$ (2 *SE*, $n = 5$) after excluding one outlier.

Supplementary Materials

The PDF file includes:
Supplementary Text
Figs. S1 to S9
Legends for tables S1 to S5
References

Other Supplementary Material for this manuscript includes the following:
Tables S1 to S5

REFERENCES AND NOTES

1. H. Jung, H. W. Green, L. F. Dobrzhinetskaya, Intermediate-depth earthquake faulting by dehydration embrittlement with negative volume change. *Nature* **428**, 545–549 (2004).
2. P. Vannucchi, F. Sage, J. P. Morgan, F. Remitti, J.-Y. Collot, Toward a dynamic concept of the subduction channel at erosive convergent margins with implications for interplate material transfer. *Geochem. Geophys. Geosyst.* **13**, Q02003 (2012).
3. T. L. Grove, N. Chatterjee, S. W. Parman, E. Médard, The influence of H2O on mantle wedge melting. *Earth Planet. Sci. Lett.* **249**, 74–89 (2006).
4. J. Gill, *Orogenic Andesites and Plate Tectonics* (Springer-Verlag, 1981).
5. M. A. Kendrick, C. Hémond, V. S. Kamenetsky, L. Danyushevsky, C. W. Devey, T. Rodemann, M. G. Jackson, M. R. Perfit, Seawater cycled throughout Earth's mantle in partially serpentinized lithosphere. *Nat. Geosci.* **10**, 222–228 (2017).
6. E. H. Hauri, J. Maclennan, D. McKenzie, K. Gronvold, N. Oskarsson, N. Shimizu, CO_2 content beneath northern Iceland and the variability of mantle carbon. *Geology* **46**, 55–58 (2017).
7. M. M. Hirschmann, Comparative deep Earth volatile cycles: The case for C recycling from exosphere/mantle fractionation of major (H_2O, C, N) volatiles and from H_2O/Ce, CO_2/Ba, and CO_2/Nb exosphere ratios. *Earth Planet. Sci. Lett.* **502**, 262–273 (2018).
8. H. W. Green, Shearing instabilities accompanying high-pressure phase transformations and the mechanics of deep earthquakes. *Proc. Natl. Acad. Sci. U.S.A.* **104**, 9133–9138 (2007).
9. H. W. Green, W.-P. Chen, M. R. Brudzinski, Seismic evidence of negligible water carried below 400-km depth in subducting lithosphere. *Nature* **467**, 828–831 (2010).
10. B. Schmandt, S. D. Jacobsen, T. W. Becker, Z. Liu, K. G. Dueker, Dehydration melting at the top of the lower mantle. *Science* **344**, 1265–1268 (2014).
11. D. Tian, S. S. Wei, W. Wang, F. Wang, Stress drops of intermediate-depth and deep earthquakes in the Tonga slab. *J. Geophys. Res. Solid Earth* **127**, e2022JB025109 (2022).
12. D. G. Pearson, F. E. Brenker, F. Nestola, J. McNeill, L. Nasdala, M. T. Hutchison, S. Matveev, K. Mather, G. Silversmit, S. Schmitz, B. Vekemans, L. Vincze, Hydrous mantle transition zone indicated by ringwoodite included within diamond. *Nature* **507**, 221–224 (2014).
13. M. J. Walter, S. C. Kohn, D. Araujo, G. P. Bulanova, C. B. Smith, E. Gaillou, J. Wang, A. Steele, S. B. Shirey, Deep mantle cycling of oceanic crust: Evidence from diamonds and their mineral inclusions. *Science* **334**, 54–57 (2011).
14. S. B. Shirey, L. S. Wagner, M. J. Walter, D. G. Pearson, P. E. van Keken, Slab transport of fluids to deep focus earthquake depths—Thermal modeling constraints and evidence from diamonds. *AGU Adv.* **2**, e2020AV000304 (2021).
15. S. B. Shirey, P. Cartigny, D. J. Frost, S. Keshav, F. Nestola, P. Nimis, D. G. Pearson, N. V. Sobolev, M. J. Walter, Diamonds and the geology of mantle carbon. *Rev. Mineral. Geochem.* **75**, 355–421 (2013).
16. V. Stagno, D. J. Frost, Carbon speciation in the asthenosphere: Experimental measurements of the redox conditions at which carbonate-bearing melts coexist with graphite or diamond in peridotite assemblages. *Earth Planet. Sci. Lett.* **300**, 72–84 (2010).
17. B. Harte, J. W. Harris, Lower mantle mineral associations preserved in diamonds. *Mineral. Mag.* **58**, 384–385 (1994).
18. B. Harte, Lower mantle mineral associations in diamonds from Sao Luiz, Brazil. *Mantle Petrology : Field Observations and High-Pressure Experimentation: A Tribute to Francis R. (Joe) Boyd* (1999), vol. 6, pp. 125–153. https://geochemsoc.org/publications/special-publications-series/v6-mantle-petrology.
19. F. Kaminsky, O. Zakharchenko, R. Davies, W. Griffin, G. Khachatryan-Blinova, A. Shiryaev, Superdeep diamonds from the Juina area, Mato Grosso State, Brazil. *Contrib. Mineral. Petrol.* **140**, 734–753 (2001).
20. M. J. Walter, G. P. Bulanova, L. S. Armstrong, S. Keshav, J. D. Blundy, G. Gudfinnsson, O. T. Lord, A. R. Lennie, S. M. Clark, C. B. Smith, L. Gobbo, Primary carbonatite melt from deeply subducted oceanic crust. *Nature* **454**, 622–625 (2008).
21. G. P. Bulanova, M. J. Walter, C. B. Smith, S. C. Kohn, L. S. Armstrong, J. Blundy, L. Gobbo, Mineral inclusions in sublithospheric diamonds from Collier 4 kimberlite pipe, Juina, Brazil: Subducted protoliths, carbonated melts and primary kimberlite magmatism. *Contrib. Mineral. Petrol.* **160**, 489–510 (2010).
22. B. Harte, Diamond formation in the deep mantle; the record of mineral inclusions and their distribution in relation to mantle dehydration zones. *Mineral. Mag.* **74**, 189–215 (2010).
23. B. Harte, S. H. Richardson, Mineral inclusions in diamonds track the evolution of a Mesozoic subducted slab beneath West Gondwanaland. *Gondw. Res.* **21**, 236–245 (2012).
24. F. Kaminsky, Mineralogy of the lower mantle: A review of 'super-deep' mineral inclusions in diamond. *Earth Sci. Rev.* **110**, 127–147 (2012).
25. B. Harte, N. F. C. Hudson, "Mineral associations in diamonds from the lowermost upper mantle and uppermost lower mantle" in *Proceedings of 10th International Kimberlite Conference* (Springer, 2013), pp. 235–253.
26. A. R. Thomson, S. C. Kohn, G. P. Bulanova, C. B. Smith, D. Araujo, EIMF, M. J. Walter, Origin of sub-lithospheric diamonds from the Juina-5 kimberlite (Brazil): Constraints from carbon isotopes and inclusion compositions. *Contrib. Mineral. Petrol.* **168**, 1081 (2014).
27. A. D. Burnham, A. R. Thomson, G. P. Bulanova, S. C. Kohn, C. B. Smith, M. J. Walter, Stable isotope evidence for crustal recycling as recorded by superdeep diamonds. *Earth Planet. Sci. Lett.* **432**, 374–380 (2015).
28. A. R. Thomson, S. C. Kohn, G. P. Bulanova, C. B. Smith, D. Araujo, M. J. Walter, Trace element composition of silicate inclusions in sub-lithospheric diamonds from the Juina-5 kimberlite: Evidence for diamond growth from slab melts. *Lithos* **265**, 108–124 (2016).
29. A. R. Thomson, M. J. Walter, S. C. Kohn, R. A. Brooker, Slab melting as a barrier to deep carbon subduction. *Nature* **529**, 76–79 (2016).
30. T. Stachel, G. P. Brey, J. W. Harris, Kankan diamonds (Guinea) I: From the lithosphere down to the transition zone. *Contrib. Mineral. Petrol.* **140**, 1–15 (2000).
31. T. Stachel, J. W. Harris, G. P. Brey, W. Joswig, Kankan diamonds (Guinea) II: Lower mantle inclusion parageneses. *Contrib. Mineral. Petrol.* **140**, 16–27 (2000).
32. T. Stachel, J. Harris, S. Aulbach, P. Deines, Kankan diamonds (Guinea) III: δ13C and nitrogen characteristics of deep diamonds. *Contrib. Mineral. Petrol.* **142**, 465–475 (2002).
33. D. G. Pearson, J. M. Scott, J. Liu, A. Schaeffer, L. H. Wang, J. van Hunen, K. Szilas, T. Chacko, P. B. Kelemen, Deep continental roots and cratons. *Nature* **596**, 199–210 (2021).
34. M. T. Hutchison, Constitution of the deep transition zone and lower mantle shown by diamonds and their inclusions. (1997).
35. E. M. W. Skinner, D. B. Apter, C. Morelli, N. K. Smithson, Kimberlites of the Man craton, West Africa. *Lithos* **76**, 233–259 (2004).
36. K. V. Smit, S. B. Shirey, W. Wang, Type Ib diamond formation and preservation in the West African lithospheric mantle: Re–Os age constraints from sulphide inclusions in Zimmi diamonds. *Precambrian Res.* **286**, 152–166 (2016).
37. S. Aulbach, H. E. Höfer, A. Gerdes, High-Mg and low-Mg mantle eclogites from Koidu (West African Craton) linked by neoproterozoic ultramafic melt metasomatism of subducted Archaean plateau-like oceanic crust. *J. Petrol.* **60**, 723–754 (2019).
38. T. M. Gernon, S. M. Jones, S. Brune, T. K. Hincks, M. R. Palmer, J. C. Schumacher, R. M. Primiceri, M. Field, W. L. Griffin, S. Y. O'Reilly, D. Keir, C. J. Spencer, A. S. Merdith,

A. Glerum, Rift-induced disruption of cratonic keels drives kimberlite volcanism. *Nature* **620**, 344–350 (2023).
39. S. Timmerman, T. Stachel, J. M. Koornneef, K. V. Smit, R. Harlou, G. M. Nowell, A. R. Thomson, S. C. Kohn, J. H. F. L. Davies, G. R. Davies, M. Y. Krebs, Q. Zhang, S. E. M. Milne, J. W. Harris, F. Kaminsky, D. Zedgenizov, G. Bulanova, C. B. Smith, I. Cabral Neto, F. V. Silveira, A. D. Burnham, F. Nestola, S. B. Shirey, M. J. Walter, A. Steele, D. G. Pearson, Sublithospheric diamond ages and the supercontinent cycle. *Nature* **623**, 752–756 (2023).
40. S. B. Shirey, D. G. Pearson, T. Stachel, M. J. Walter, Sublithospheric diamonds: Plate tectonics from Earth's deepest mantle samples. *Annu. Rev. Earth Planet. Sci.* **52**, 249–293 (2024).
41. M. J. Walter, A. R. Thomson, E. M. Smith, Geochemistry of silicate and oxide inclusions in sublithospheric diamonds. *Rev. Mineral. Geochem.* **88**, 393–450 (2022).
42. N. A. Meyer, T. Stachel, D. G. Pearson, R. A. Stern, J. W. Harris, M. J. Walter, Diamonds reveal subducted slab harzburgite in the lower mantle. *Geology* **51**, 238–241 (2023).
43. T. Stachel, P. Cartigny, T. Chacko, D. G. Pearson, Carbon and nitrogen in mantle-derived diamonds. *Rev. Mineral. Geochem.* **88**, 809–875 (2022).
44. F.-Z. Teng, W.-Y. Li, S. Ke, B. Marty, N. Dauphas, S. Huang, F.-Y. Wu, A. Pourmand, Magnesium isotopic composition of the Earth and chondrites. *Geochim. Cosmochim. Acta* **74**, 4150–4166 (2010).
45. T. Ishii, H. Kojitani, M. Akaogi, Phase relations and mineral chemistry in pyrolitic mantle at 1600–2200 °C under pressures up to the uppermost lower mantle: Phase transitions around the 660-km discontinuity and dynamics of upwelling hot plumes. *Phys. Earth Planet. In.* **274**, 127–137 (2018).
46. T. Ishii, H. Kojitani, M. Akaogi, Phase relations of Harzburgite and MORB up to the uppermost lower mantle conditions: Precise comparison with pyrolite by multisample cell high-pressure experiments with implication to dynamics of subducted slabs. *J. Geophys. Res. Solid Earth* **124**, 3491–3507 (2019).
47. A. M. Dziewonski, D. L. Anderson, Preliminary reference Earth model. *Phys. Earth Planet. In.* **25**, 297–356 (1981).
48. H. Iwamori, Phase relations of peridotites under H2O-saturated conditions and ability of subducting plates for transportation of H_2O. *Earth Planet. Sci. Lett.* **227**, 57–71 (2004).
49. T. Komabayashi, S. Omori, Internally consistent thermodynamic data set for dense hydrous magnesium silicates up to 35GPa, 1600°C: Implications for water circulation in the Earth's deep mantle. *Phys. Earth Planet. In.* **156**, 89–107 (2006).
50. L. Liu, An alternative interpretation of lower mantle mineral associations in diamonds. *Contrib. Mineral. Petrol.* **144**, 16–21 (2002).
51. G. P. Brey, V. Bulatov, A. Girnis, J. W. Harris, T. Stachel, Ferropericlase—A lower mantle phase in the upper mantle. *Lithos* **77**, 655–663 (2004).
52. K. Li, L. Li, D. G. Pearson, T. Stachel, Diamond isotope compositions indicate altered igneous oceanic crust dominates deep carbon recycling. *Earth Planet. Sci. Lett.* **516**, 190–201 (2019).
53. E. M. Smith, P. Ni, S. B. Shirey, S. H. Richardson, W. Wang, A. Shahar, Heavy iron in large gem diamonds traces deep subduction of serpentinized ocean floor. *Sci. Adv.* **7**, eabe9773 (2021).
54. F.-Z. Teng, Magnesium isotope geochemistry. *Rev. Mineral. Geochem.* **82**, 219–287 (2017).
55. P. Cartigny, M. Palot, E. Thomassot, J. W. Harris, Diamond formation: A stable isotope perspective. *Annu. Rev. Earth Planet. Sci.* **42**, 699–732 (2014).
56. P. B. Kelemen, C. E. Manning, Reevaluating carbon fluxes in subduction zones, what goes down, mostly comes up. *Proc. Natl. Acad. Sci. U.S.A.* **112**, E3997–E4006 (2015).
57. E. S. Kiseeva, N. Korolev, I. Koemets, D. A. Zedgenizov, R. Unitt, C. McCammon, A. Aslandukova, S. Khandarkhaeva, T. Fedotenko, K. Glazyrin, D. Bessas, G. Aprilis, A. I. Chumakov, H. Kagi, L. Dubrovinsky, Subduction-related oxidation of the sublithospheric mantle evidenced by ferropericlase and magnesiowüstite diamond inclusions. *Nat. Commun.* **13**, 7517 (2022).
58. D. J. Schulze, B. Harte, J. W. Valley, D. M. DeR, Channer, Evidence of subduction and crust–mantle mixing from a single diamond. *Lithos* **77**, 349–358 (2004).
59. P. R. Craddock, J. M. Warren, N. Dauphas, Abyssal peridotites reveal the near-chondritic Fe isotopic composition of the Earth. *Earth Planet. Sci. Lett.* **365**, 63–76 (2013).
60. P. A. Sossi, O. Nebel, J. Foden, Iron isotope systematics in planetary reservoirs. *Earth Planet. Sci. Lett.* **452**, 295–308 (2016).
61. S. Lorenzon, M. Wenz, P. Nimis, S. D. Jacobsen, L. Pasqualetto, M. G. Pamato, D. Novella, D. Zhang, C. Anzolini, M. Regier, T. Stachel, D. G. Pearson, J. W. Harris, F. Nestola, Dual origin of ferropericlase inclusions within super-deep diamonds. *Earth Planet. Sci. Lett.* **608**, 118081 (2023).
62. M. Bruno, S. Ghignone, D. Aquilano, F. Nestola, A critique of using epitaxial criterion to discriminate between protogenetic and syngenetic mineral inclusions in diamond. *Sci. Rep.* **14**, 8674 (2024).
63. C. R. Soderman, S. Matthews, O. Shorttle, M. G. Jackson, J. M. D. Day, V. Kamenetsky, H. M. Williams, Global oceanic basalt sources and processes viewed through combined Fe and Mg stable isotopes. *Earth Planet. Sci. Lett.* **638**, 118749 (2024).
64. X.-N. Liu, R. C. Hin, C. D. Coath, M. Bizimis, L. Su, D. A. Ionov, E. Takazawa, R. Brooker, T. Elliott, The magnesium isotopic composition of the mantle. *Geochim. Cosmochim. Acta* **358**, 12–26 (2023).
65. K.-J. Huang, F.-Z. Teng, T. Plank, H. Staudigel, Y. Hu, Z.-Y. Bao, Magnesium isotopic composition of altered oceanic crust and the global Mg cycle. *Geochim. Cosmochim. Acta* **238**, 357–373 (2018).
66. E. A. Schauble, First-principles estimates of equilibrium magnesium isotope fractionation in silicate, oxide, carbonate and hexaaquamagnesium(2+) crystals. *Geochim. Cosmochim. Acta* **75**, 844–869 (2011).
67. S.-J. Wang, F.-Z. Teng, H. M. Williams, S.-G. Li, Magnesium isotopic variations in cratonic eclogites: Origins and implications. *Earth Planet. Sci. Lett.* **359–360**, 219–226 (2012).
68. S.-J. Wang, F.-Z. Teng, R. L. Rudnick, S.-G. Li, Magnesium isotope evidence for a recycled origin of cratonic eclogites. *Geology* **43**, 1071–1074 (2015).
69. J.-X. Huang, Y. Xiang, Y. An, W. L. Griffin, Y. Gréau, L. Xie, N. J. Pearson, H. Yu, S. Y. O'Reilly, Magnesium and oxygen isotopes in Roberts Victor eclogites. *Chem. Geol.* **438**, 73–83 (2016).
70. W. Yang, F.-Z. Teng, H.-F. Zhang, S.-G. Li, Magnesium isotopic systematics of continental basalts from the North China craton: Implications for tracing subducted carbonate in the mantle. *Chem. Geol.* **328**, 185–194 (2012).
71. H.-C. Tian, W. Yang, S.-G. Li, S. Ke, Z.-Y. Chu, Origin of low δ26Mg basalts with EM-I component: Evidence for interaction between enriched lithosphere and carbonated asthenosphere. *Geochim. Cosmochim. Acta* **188**, 93–105 (2016).
72. B.-X. Su, Y. Hu, F.-Z. Teng, Y. Xiao, X.-H. Zhou, Y. Sun, M.-F. Zhou, S.-C. Chang, Magnesium isotope constraints on subduction contribution to Mesozoic and Cenozoic East Asian continental basalts. *Chem. Geol.* **466**, 116–122 (2017).
73. Y. Xiao, F.-Z. Teng, H.-F. Zhang, W. Yang, Large magnesium isotope fractionation in peridotite xenoliths from eastern North China craton: Product of melt–rock interaction. *Geochim. Cosmochim. Acta* **115**, 241–261 (2013).
74. Y. Hu, F.-Z. Teng, H.-F. Zhang, Y. Xiao, B.-X. Su, Metasomatism-induced mantle magnesium isotopic heterogeneity: Evidence from pyroxenites. *Geochim. Cosmochim. Acta* **185**, 88–111 (2016).
75. L. Ternieten, G. L. Früh-Green, S. M. Bernasconi, Carbonate mineralogy in mantle peridotites of the Atlantis Massif (IODP Expedition 357). *J. Geophys. Res. Solid Earth* **126**, e2021JB021885 (2021).
76. L. Ternieten, G. L. Früh-Green, S. M. Bernasconi, Distribution and sources of carbon in serpentinized mantle peridotites at the Atlantis Massif (IODP Expedition 357). *J. Geophys. Res. Solid Earth* **126**, e2021JB021973 (2021).
77. F. V. Kaminsky, D. A. Zedgenizov, V. S. Sevastyanov, O. V. Kuznetsova, Distinct groups of low- and high-Fe ferropericlase inclusions in super-deep diamonds: An example from the Juina Area, Brazil. *Minerals* **13**, 1217 (2023).
78. L. D. V. Carvalho, T. Stachel, R. W. Luth, A. J. Locock, D. G. Pearson, M. Steele-MacInnis, R. A. Stern, F. Nestola, R. Scholz, T. Jalowitzki, R. A. Fuck, Dense hydrated Mg-silicates in diamond: Implications for transport of H_2O into the mantle. *Sci. Adv.* **10**, eadl4306 (2024).
79. J.-W. Xiong, Y.-X. Chen, M. Scambelluri, X.-Y. Qiao, Y. Chen, F. Huang, D. Belmonte, Z.-F. Zhao, Fluid-metasomatized rocks with extremely low δ^{26}Mg values in subducted oceanic lithosphere: Implications for mantle Mg isotope heterogeneity and the origin of low-δ^{26}Mg magmas. *Geochim. Cosmochim. Acta* **371**, 111–125 (2024).
80. I. Grevemeyer, N. W. Hayman, C. Peirce, M. Schwardt, H. J. A. Van Avendonk, A. Dannowski, C. Papenberg, Episodic magmatism and serpentinized mantle exhumation at an ultraslow-spreading centre. *Nat. Geosci.* **11**, 444–448 (2018).
81. M. Faccenda, Water in the slab: A trilogy. *Tectonophysics* **614**, 1–30 (2014).
82. A. Nakajima, T. Sakamaki, T. Kawazoe, A. Suzuki, Hydrous magnesium-rich magma genesis at the top of the lower mantle. *Sci. Rep.* **9**, 7420 (2019).
83. R. Huang, T. Boffa Ballaran, C. A. McCammon, D. J. Frost, The composition and redox state of hydrous partial melts generated at the top of the lower mantle. *Earth Planet. Sci. Lett.* **624**, 118447 (2023).
84. L. Xie, M. Walter, T. Katsura, F. Xu, J. Wang, Y. Fei, Crystallization of a hydrous magma ocean in the shallow lower mantle. *Earth Planet. Sci. Lett.* **633**, 118651 (2024).
85. C. R. Ranero, J. P. Morgan, K. McIntosh, C. Reichert, Bending-related faulting and mantle serpentinization at the Middle America trench. *Nature* **425**, 367–373 (2003).
86. B. R. Frost, On the stability of sulfides, oxides, and native metals in serpentinite. *J. Petrol.* **26**, 31–63 (1985).
87. F. Klein, W. Bach, N. Jöns, T. McCollom, B. Moskowitz, T. Berquó, Iron partitioning and hydrogen generation during serpentinization of abyssal peridotites from 15°N on the Mid-Atlantic Ridge. *Geochim. Cosmochim. Acta* **73**, 6868–6893 (2009).
88. S. R. Scott, K. W. W. Sims, B. R. Frost, P. B. Kelemen, K. A. Evans, S. M. Swapp, On the hydration of olivine in ultramafic rocks: Implications from Fe isotopes in serpentinites. *Geochim. Cosmochim. Acta* **215**, 105–121 (2017).
89. M. Scambelluri, E. Cannaò, M. Gilio, The water and fluid-mobile element cycles during serpentinite subduction. A review. *Eur. J. Mineral.* **31**, 405–428 (2019).
90. H. J. A. V. Avendonk, W. S. Holbrook, D. Lizarralde, P. Denyer, Structure and serpentinization of the subducting Cocos plate offshore Nicaragua and Costa Rica. *Geochem. Geophys. Geosyst.* **12**, doi.org/10.1029/2011GC003592 (2011).
91. F. Nestola, M. E. Regier, R. W. Luth, D. G. Pearson, T. Stachel, C. McCammon, M. D. Wenz, S. D. Jacobsen, C. Anzolini, L. Bindi, J. W. Harris, Extreme redox variations in a superdeep diamond from a subducted slab. *Nature* **613**, 85–89 (2023).

92. J. W. E. Drewitt, M. J. Walter, J. P. Brodholt, J. M. R. Muir, O. T. Lord, Hydrous silicate melts and the deep mantle H_2O cycle. *Earth Planet. Sci. Lett.* **581**, 117408 (2022).
93. M. J. Walter, E. Nakamura, R. G. Trønnes, D. J. Frost, Experimental constraints on crystallization differentiation in a deep magma ocean. *Geochim. Cosmochim. Acta* **68**, 4267–4284 (2004).
94. T. Nakagawa, P. J. Tackley, F. Deschamps, J. A. D. Connolly, The influence of MORB and harzburgite composition on thermo-chemical mantle convection in a 3-D spherical shell with self-consistently calculated mineral physics. *Earth Planet. Sci. Lett.* **296**, 403–412 (2010).
95. L. Stixrude, C. Lithgow-Bertelloni, Geophysics of chemical heterogeneity in the mantle. *Annu. Rev. Earth Planet. Sci.* **40**, 569–595 (2012).
96. G. L. Früh-Green, D. S. Kelley, M. D. Lilley, M. Cannat, V. Chavagnac, J. A. Baross, Diversity of magmatism, hydrothermal processes and microbial interactions at mid-ocean ridges. *Nat. Rev. Earth Environ.* **3**, 852–871 (2022).
97. C. H. Langmuir, E. M. Klein, T. Plank, "Petrological systematics of mid-ocean ridge basalts: Constraints on melt generation beneath ocean ridges" in *Mantle Flow and Melt Generation at Mid-Ocean Ridges* [American Geophysical Union (AGU), 1992; https://onlinelibrary.wiley.com/doi/abs/10.1029/GM071p0183], pp. 183–280.
98. E. M. Smith, S. B. Shirey, F. Nestola, E. S. Bullock, J. Wang, S. H. Richardson, W. Wang, Large gem diamonds from metallic liquid in Earth's deep mantle. *Science* **354**, 1403–1405 (2016).
99. M. D. Wenz, S. D. Jacobsen, D. Zhang, M. Regier, H. J. Bausch, P. K. Dera, M. Rivers, P. Eng, S. B. Shirey, D. G. Pearson, Fast identification of mineral inclusions in diamond at GSECARS using synchrotron x-ray microtomography, radiography and diffraction. *J. Synchrotron Rad.* **26**, 1763–1768 (2019).
100. C. Anzolini, F. Nestola, M. L. Mazzucchelli, M. Alvaro, P. Nimis, A. Gianese, S. Morganti, F. Marone, M. Campione, M. T. Hutchison, J. W. Harris, Depth of diamond formation obtained from single periclase inclusions. *Geology* **47**, 219–222 (2019).
101. P. R. Craddock, N. Dauphas, Iron isotopic compositions of geological reference materials and chondrites. *Geostand. Geoanal. Res.* **35**, 101–123 (2010).
102. P. Ni, N. L. Chabot, C. J. Ryan, A. Shahar, Heavy iron isotope composition of iron meteorites explained by core crystallization. *Nat. Geosci.* **13**, 611–615 (2020).
103. M. L. M. Gleeson, S. A. Gibson, H. M. Williams, Novel insights from Fe-isotopes into the lithological heterogeneity of ocean island basalts and plume-influenced MORBs. *Earth Planet. Sci. Lett.* **535**, 116114 (2020).
104. F.-Z. Teng, N. Dauphas, S. Huang, B. Marty, Iron isotopic systematics of oceanic basalts. *Geochim. Cosmochim. Acta* **107**, 12–26 (2013).
105. N. Dauphas, S. G. John, O. Rouxel, Iron isotope systematics. *Rev. Mineral. Geochem.* **82**, 415–510 (2017).
106. H. M. Williams, M. Bizimis, Iron isotope tracing of mantle heterogeneity within the source regions of oceanic basalts. *Earth Planet. Sci. Lett.* **404**, 396–407 (2014).
107. F. Poitrasson, A. N. Halliday, D.-C. Lee, S. Levasseur, N. Teutsch, Iron isotope differences between Earth, Moon, Mars and Vesta as possible records of contrasted accretion mechanisms. *Earth Planet. Sci. Lett.* **223**, 253–266 (2004).
108. S. Weyer, A. D. Anbar, G. P. Brey, C. Münker, K. Mezger, A. B. Woodland, Iron isotope fractionation during planetary differentiation. *Earth Planet. Sci. Lett.* **240**, 251–264 (2005).
109. R. Schoenberg, F. von Blanckenburg, Modes of planetary-scale Fe isotope fractionation. *Earth Planet. Sci. Lett.* **252**, 342–359 (2006).
110. O. Nebel, P. A. Sossi, A. Bénard, M. Wille, P. Z. Vroon, R. J. Arculus, Redox-variability and controls in subduction zones from an iron-isotope perspective. *Earth Planet. Sci. Lett.* **432**, 142–151 (2015).
111. J. Foden, P. A. Sossi, O. Nebel, Controls on the iron isotopic composition of global arc magmas. *Earth Planet. Sci. Lett.* **494**, 190–201 (2018).
112. S. Chen, Y. Niu, P. Guo, H. Gong, P. Sun, Q. Xue, M. Duan, X. Wang, Iron isotope fractionation during mid-ocean ridge basalt (MORB) evolution: Evidence from lavas on the East Pacific Rise at 10°30′N and its implications. *Geochim. Cosmochim. Acta* **267**, 227–239 (2019).
113. O. Nebel, P. A. Sossi, A. Bénard, R. J. Arculus, G. M. Yaxley, J. D. Woodhead, D. Rhodri Davies, S. Ruttor, Reconciling petrological and isotopic mixing mechanisms in the Pitcairn mantle plume using stable Fe isotopes. *Earth Planet. Sci. Lett.* **521**, 60–67 (2019).
114. B. J. Peters, A. Shahar, R. W. Carlson, J. M. D. Day, T. D. Mock, A sulfide perspective on iron isotope fractionation during ocean island basalt petrogenesis. *Geochim. Cosmochim. Acta* **245**, 59–78 (2019).
115. B.-X. Su, F.-Z. Teng, Y. Hu, R.-D. Shi, M.-F. Zhou, B. Zhu, F. Liu, X.-H. Gong, Q.-S. Huang, Y. Xiao, C. Chen, Y.-S. He, Iron and magnesium isotope fractionation in oceanic lithosphere and sub-arc mantle: Perspectives from ophiolites. *Earth Planet. Sci. Lett.* **430**, 523–532 (2015).
116. F.-Z. Teng, W.-Y. Li, S. Ke, W. Yang, S.-A. Liu, F. Sedaghatpour, S.-J. Wang, K.-J. Huang, Y. Hu, M.-X. Ling, Y. Xiao, X.-M. Liu, X.-W. Li, H.-O. Gu, C. K. Sio, D. A. Wallace, B.-X. Su, L. Zhao, J. Chamberlin, M. Harrington, A. Brewer, Magnesium isotopic compositions of international geological reference materials. *Geostand. Geoanal. Res.* **39**, 329–339 (2015).
117. A. Galy, M. Bar-Matthews, L. Halicz, R. K. O'Nions, Mg isotopic composition of carbonate: Insight from speleothem formation. *Earth Planet. Sci. Lett.* **201**, 105–115 (2002).
118. V. T.-C. Chang, A. Makishima, N. S. Belshaw, R. Keith O'Nions, Purification of Mg from low-Mg biogenic carbonates for isotope ratio determination using multiple collector ICP-MS. *J. Anal. At. Spectrom* **18**, 296–301 (2003).
119. A. Brenot, C. Cloquet, N. Vigier, J. Carignan, C. France-Lanord, Magnesium isotope systematics of the lithologically varied Moselle river basin, France. *Geochim. Cosmochim. Acta* **72**, 5070–5089 (2008).
120. F. Wombacher, A. Eisenhauer, A. Heuser, S. Weyer, Separation of Mg, Ca and Fe from geological reference materials for stable isotope ratio analyses by MC-ICP-MS and double-spike TIMS. *J. Anal. At. Spectrom* **24**, 627–636 (2009).
121. A. D. Jacobson, Z. Zhang, C. Lundstrom, F. Huang, Behavior of Mg isotopes during dedolomitization in the Madison Aquifer, South Dakota. *Earth Planet. Sci. Lett.* **297**, 446–452 (2010).
122. J. A. Higgins, D. P. Schrag, Constraining magnesium cycling in marine sediments using magnesium isotopes. *Geochim. Cosmochim. Acta* **74**, 5039–5053 (2010).
123. M. S. Fantle, J. Higgins, The effects of diagenesis and dolomitization on Ca and Mg isotopes in marine platform carbonates: Implications for the geochemical cycles of Ca and Mg. *Geochim. Cosmochim. Acta* **142**, 458–481 (2014).
124. C. L. Blättler, N. R. Miller, J. A. Higgins, Mg and Ca isotope signatures of authigenic dolomite in siliceous deep-sea sediments. *Earth Planet. Sci. Lett.* **419**, 32–42 (2015).
125. M. E. Regier, D. G. Pearson, T. Stachel, R. W. Luth, R. A. Stern, J. W. Harris, The lithospheric-to-lower-mantle carbon cycle recorded in superdeep diamonds. *Nature* **585**, 234–238 (2020).
126. K. A. Evans, B. R. Frost, Deserpentinization in subduction zones as a source of oxidation in arcs: A reality check. *J. Petrol.* **62**, egab016 (2020).
127. S. K. Birner, E. Cottrell, F. A. Davis, J. M. Warren, Deep, hot, ancient melting recorded by ultralow oxygen fugacity in peridotites. *Nature* **631**, 801–807 (2024).
128. L. Libon, G. Spiekermann, I. Blanchard, J. M. Kaa, S. Dominijanni, M. J. Sieber, M. Förster, C. Albers, W. Morgenroth, C. McCammon, A. Schreiber, V. Roddatis, K. Glazyrin, R. J. Husband, L. Hennet, K. Appel, M. Wilke, Reevaluating the fate of subducted magnesite in the Earth's lower mantle. *Phys. Earth Planet. In.* **355**, 107238 (2024).

Acknowledgments: T. Mock is acknowledged for assistance with the mass spectrometry. We thank F.-Z. Teng for providing the Mg isotope standard. **Funding:** This work received support from the US National Science Foundation award EAR-2025779 (S.B.S., A.Sh., and M.J.W.), US National Science Foundation award EAR-1853521 (S.D.J.), Canada Research Chair program CRC-2018-00318 (T.S.), Carnegie Canada Foundation (N.K.), and Rita Levi Montalcini Program of the Italian Ministry of University and Research (D.N.). **Author contributions:** Conceptualization: P.N., S.B.S., M.J.W., E.M.S., A.Sh., and N.K. Sample selection: P.N., J.C., S.B.S., D.N., F.N., T.S., D.G.P., L.L.G., S.D.J., B.H., and J.W.H. Methodology: P.N., A.St., E.M.S., S.B.S., and N.K. Investigation: P.N., J.C., D.N., F.N., N.K., and A.St. Visualization: P.N. and M.J.W. Writing—original draft: P.N., S.B.S., and M.J.W. Writing—review and editing: P.N., S.B.S., M.J.W., J.C., D.N., F.N., N.K., E.M.S., T.S., D.G.P., A.Sh., L.L.G., S.D.J., and J.W.H. **Competing interests:** The authors declare that they have no competing interests. **Data and materials availability:** All data needed to evaluate the conclusions in the paper are present in the paper and/or the Supplementary Materials.

Submitted 16 October 2024
Accepted 19 September 2025
Published 15 October 2025
10.1126/sciadv.adt9106

ScienceAdvances

Onset of slab mantle melting in Earth's lower mantle: Evidence from ferropericlase in superdeep diamonds

Peng Ni, Steven B. Shirey, Michael J. Walter, Janina Czas, Davide Novella, Fabrizio Nestola, Nico Kueter, Evan M. Smith, Thomas Stachel, D. Graham Pearson, Andrew Steele, Laura L. Gardner, Steven D. Jacobsen, Ben Harte, Jeffrey W. Harris, and Anat Shahar

Sci. Adv. **11** (42), eadt9106. DOI: 10.1126/sciadv.adt9106

Science Advances (ISSN 2375-2548) is published by the American Association for the Advancement of Science. 1200 New York Avenue NW, Washington, DC 20005. The title *Science Advances* is a registered trademark of AAAS.